Monthly Notices
of the
ROYAL ASTRONOMICAL SOCIETY

MNRAS **491,** 5595–5620 (2020)
Advance Access publication 2019 November 28

doi:10.1093/mnras/stz3296

Formation of compact systems of super-Earths via dynamical instabilities and giant impacts

Sanson T. S. Poon,[1,2]★ Richard P. Nelson,[1] Seth A. Jacobson[3] and Alessandro Morbidelli[4]

[1]*Astronomy Unit, Queen Mary University of London, London E1 4NS, UK*
[2]*Royal Observatory Greenwich, London SE10 9NF, UK*
[3]*Earth and Planetary Sciences, Northwestern University, Evanston, Illinois 60208-3130, USA*
[4]*Observatoire de la Côte d'Azur, Laboratoire Lagrange, Bd. de l'Observatoire, CS 34229, F-06304 Nice Cedex 4, France*

Accepted 2019 November 19. Received 2019 October 8; in original form 2019 August 5

ABSTRACT

The NASA's Kepler mission discovered ∼700 planets in multiplanet systems containing three or more transiting bodies, many of which are super-Earths and mini-Neptunes in compact configurations. Using *N*-body simulations, we examine the *in situ*, final stage assembly of multiplanet systems via the collisional accretion of protoplanets. Our initial conditions are constructed using a subset of the Kepler five-planet systems as templates. Two different prescriptions for treating planetary collisions are adopted. The simulations address numerous questions: Do the results depend on the accretion prescription?; do the resulting systems resemble the Kepler systems, and do they reproduce the observed distribution of planetary multiplicities when synthetically observed?; do collisions lead to significant modification of protoplanet compositions, or to stripping of gaseous envelopes?; do the eccentricity distributions agree with those inferred for the Kepler planets? We find that the accretion prescription is unimportant in determining the outcomes. The final planetary systems look broadly similar to the Kepler templates adopted, but the observed distributions of planetary multiplicities or eccentricities are not reproduced, because scattering does not excite the systems sufficiently. In addition, we find that ∼1 per cent of our final systems contain a co-orbital planet pair in horseshoe or tadpole orbits. Post-processing the collision outcomes suggests that they would not significantly change the ice fractions of initially ice-rich protoplanets, but significant stripping of gaseous envelopes appears likely. Hence, it may be difficult to reconcile the observation that many low-mass Kepler planets have H/He envelopes with an *in situ* formation scenario that involves giant impacts after dispersal of the gas disc.

Key words: planets and satellites: composition – planets and satellites: dynamical evolution and stability – planets and satellites: formation.

1 INTRODUCTION

The Kepler mission discovered 4723 exoplanet candidates, of which 2302 have been confirmed as bona fide transiting planets (Borucki et al. 2010, 2011; Batalha et al. 2013; Burke et al. 2014; Mullally et al. 2015; Rowe et al. 2015; Coughlin et al. 2016; Thompson et al. 2018). More than 70 per cent of Kepler planets have radii $1\,R_\oplus \leq R_p \leq 4\,R_\oplus$, such that super-Earths and mini-Neptunes make up a large fraction of the known exoplanet population.[1] A significant number of these planets are found in compact multiplanet systems, such as the six-planet system Kepler-11 (Lissauer et al. 2011b) and the five-planet system Kepler-84 (Rowe et al. 2014). The highest multiplicity system detected by Kepler where all planets are confirmed is Kepler-90, with eight planets transiting its host star (Shallue & Vanderburg 2018). Analyses of the Kepler data to determine occurrence rates of planets show that systems of Earths and super-Earths with orbital periods <100 d are common around solar-type stars (e.g. Fressin et al. 2013; Petigura, Howard & Marcy 2013). A recent analysis suggests that the mean multiplicity of super-Earth systems with periods <100 d is ∼3, approximately 1/3 of Sun-like stars host compact planetary systems, and the mean number of planets per star is ∼1 (Zhu et al. 2018).

The relative numbers of one- to eight-planet systems discovered via transit detections are dependent on both the intrinsic multiplicities of the systems, and the mutual orbital inclinations of the planets

★ E-mail: s.t.s.poon@qmul.ac.uk

[1]All Kepler planetary data used in this paper are from NASA Exoplanet Archive unless stated otherwise.

that comprise the systems. In this work, we examine whether or not a simple model of the *in situ*, final stage assembly of planetary systems, involving dynamical instabilities and accretion through giant impacts among a large population of protoplanets after the gaseous protoplanetary disc has dispersed, is consistent with the Kepler observations.

Previous *N*-body simulations have considered the formation of compact systems of planets from an earlier stage than we consider here, and include the influence of the protoplanetary disc and subsequent disc–planet interactions (e.g. Terquem & Papaloizou 2007; Hellary & Nelson 2012; Coleman & Nelson 2014; Cossou et al. 2014; Coleman & Nelson 2016). One feature of these simulations is that chains of short-period planets in mean motion resonances are a common outcome, contrary to what is observed in the Kepler planet population. More recent work, however, has indicated that these resonant chains can become dynamically unstable once the gas disc has dispersed, such that the final stages of planetary assembly involve mutual scattering and collisions between planets (Matsumoto, Nagasawa & Ida 2012; Izidoro et al. 2017, 2019; Carrera, Ford & Izidoro 2019). In addition to breaking the resonant chains, the gravitational scattering also raises the mutual inclinations and eccentricities, and allows under some circumstances for the simulations to produce planetary system multiplicities that are reported to be in agreement with the Kepler data.

In contrast to the migration-driven formation scenario described above, there have also been *N*-body studies of *in situ* formation in a gas-free environment (e.g. Hansen & Murray 2012; Moriarty & Ballard 2016; Matsumoto & Kokubo 2017). Here, the initial conditions consist of numerous protoplanets arranged in an annulus that undergo mutual scatterings and collisions on the way to assembling the final systems. While these calculations are in some ways similar to the final stages of the migration-driven scenarios when the breakup of the resonant chains occurs, they differ in some important respects. For example, the planets do not start in resonance, and the number of bodies involved in the collisional evolution is significantly larger. Hence, the number of collisions experienced by a typical planet is also larger during the evolution.

Our approach in this paper is similar to that used in the aforementioned *in situ* models, except we use a subset of the Kepler five-planet systems as templates when constructing the initial conditions of the *N*-body simulations. We reconstruct the surface density distributions of the chosen planetary systems, and use this to define initial conditions consisting of numerous orbiting protoplanets. The approach is therefore similar to the construction of a minimum-mass exoplanet nebula model proposed by Chiang & Laughlin (2013). The protoplanet systems are then evolved for 10^7 yr in a gas-free environment. For each of the planetary systems we consider, we perform two sets of simulations. One uses a traditional hit-and-stick accretion prescription when collisions occur, and the other uses a more complex accretion prescription based on hydrodynamical simulations of colliding bodies (Leinhardt & Stewart 2012). Hence, we are able to examine the influence of the accretion prescription on the outcomes of the simulations, similar to the recent study by Mustill, Davies & Johansen (2018).

Adopting a more complex collision model also allows us to track the impact energy during collisions, and we use this information to examine possible composition changes that the planets could potentially experience through the removal of volatile components. Using the relations between the collision energy and the final water content of the largest remnant after differentiated bodies composed of rock and water have collided (Stewart & Leinhardt 2009; Marcus et al. 2010), we determine how much water could be removed from the planets during their collisional evolution. Although some individual collisions would likely lead to significant compositional changes, taken as a whole our results indicate that the compositions of water-rich super-Earths would not change significantly, if their final stages of evolution were similar to those occurring in the simulations. A similar analysis was also used to examine whether or not the impact energies during collisions could potentially remove putative H/He envelopes from the planets, by the conversion of impact energy into heat energy in the cores (Biersteker & Schlichting 2019), and here we find that very significant erosion of gaseous envelopes should be expected.

The rest of this paper is structured as follows. In Section 2, we describe the simulation methods and the set-up of the initial conditions. In Section 3, we present the main outcomes of our simulations, and in Section 4 we examine the formation pathways of the co-orbital planets that arise in the simulations. In Section 5, we post-process the simulation data and examine the changes to compositions that might arise during collisions, and in Section 6 we examine the stripping of gaseous envelopes that might arise. In Section 7, we discuss the results from synthetic observation of the final simulated systems, and examine in particular the distribution of system multiplicities and eccentricities that arises. Finally, we discuss our results and draw conclusions in Section 8.

2 *N*-BODY SIMULATION METHODS

We use the *N*-body codes `mercury` (Chambers 1999) and `symba` (Duncan, Levison & Lee 1998) to undertake the simulations presented in this paper. Both the codes use the Mixed Variable Symplectic (MVS) integration scheme (Wisdom & Holman 1991), but whereas `mercury` handles close encounters by transitioning to a Bulirsch–Stoer method (Press et al. 1992), `symba` uses the regularized MVS scheme (Levison & Duncan 1994). More importantly, for the work presented here, the versions of the two codes we employ handle collisions differently. `mercury` uses a simple hit-and-stick algorithm that conserves the total mass and linear momentum when two bodies collide and accrete into a single object, whereas our version of `symba` adopts the imperfect accretion algorithm from Leinhardt & Stewart (2012), which we describe below.

2.1 Imperfect collision model

For a detailed description of the Leinhardt & Stewart (2012) collision model, we refer the reader to that paper, and here we simply summarize the post-collision outcomes that are generated by it, along with a few salient details about the implementation. We note that the collision model was implemented in `symba` by the authors.[2] We refer to the more massive body involved in the collision as the target, and the less massive object as the projectile. The range of outcomes includes the following: a perfect merger where a single body is formed with the total mass and momentum of the original two bodies; a single massive body remains whose (largest remnant) mass is denoted as $M_{\rm LR}$, along with collisional debris in the form of low-mass 'superplanetesimals' (gravitating particles that are not mutually interacting); two massive bodies remain with masses $M_{\rm LR}$

[2]We warmly acknowledge the assistance of Zoe Leinhardt in this implementation during a visit to the Observatoire de la Côte d'Azur.

and $M_{\rm SLR}$ (mass of the second largest remnant), along with collision debris in the form of low-mass 'superparticles'; no massive bodies remain and all the mass is in the form of collision debris represented by low-mass 'superplanetesimals'. The following notation is used in the description below: $V_{\rm imp}$ is the impact velocity; $V_{\rm esc}$ is the escape velocity from the colliding bodies (or, more accurately, from the combined target mass and interacting mass of the projectile); $Q_{\rm R}$ is the impact energy; $Q^*_{\rm RD}$ is the catastrophic disruption energy, which by definition corresponds to the impact energy when the mass of the largest remnant contains half of the total mass of the colliding bodies; $b_{\rm crit}$ is the critical impact parameter that determines whether or not a collision is grazing ($b \geq b_{\rm crit}$) or non-grazing ($b < b_{\rm crit}$). The collision algorithm consists of a decision tree with the following possible outcomes:

(i) When $V_{\rm imp} < V_{\rm esc}$, we have a perfect merger.
(ii) When $V_{\rm imp}$ exceeds the threshold for supercatastrophic disruption, both colliding bodies are destroyed and only collisional debris remains.
(iii) When $V_{\rm imp}$ exceeds the threshold for catastrophic disruption or erosion, only one massive body remains and the rest of the mass is in the form of collisional debris. Here, $M_{\rm LR}$, the mass of the largest post-collision remnant, depends on $Q_{\rm R}$ and $Q^*_{\rm RD}$.
(iv) If $V_{\rm imp}$ is smaller than the threshold for erosion and $b < b_{\rm crit}$, then we have partial accretion where the target body gains mass from the projectile, which is itself completely disrupted into a number of low-mass 'superplanetesimals'. $M_{\rm LR}$ again depends on $Q_{\rm R}$ and $Q^*_{\rm RD}$.
(v) For $b \geq b_{\rm crit}$, in descending order of the impact velocities, we have the following outcomes that all preserve the mass of the target object and modify the mass of the projectile: hit-and-spray, where the projectile is completely disrupted into debris particles; hit-and-run, where the projectile mass is reduced and the remaining mass goes into debris particles; bouncing collision, where the projectile retains all of its mass and the collision is treated as an inelastic bounce; graze-and-merge collision, where a single body forms containing all the mass of the colliding objects.

The total mass before and after a collision, $M_{\rm Total}$, is conserved, which means that the total mass of the post-collision bodies obeys the relation $M_{\rm T,\,d} = M_{\rm Total} - (M_{\rm LR} + M_{\rm SLR})$, where $M_{\rm T,\,d}$ is the total mass in debris after the collision. The number of debris particles, $N_{\rm d}$, is given by

$$N_{\rm d} = \begin{cases} \max\left(\dfrac{M_{\rm T,d}}{10.0{\rm M_{Ceres}}}, \min\left(38, \dfrac{M_{\rm T,d}}{0.1{\rm M_{Ceres}}}\right)\right), & \text{if } M_{\rm T,d} > 0 \\ 0, & \text{otherwise} \end{cases} \tag{1}$$

where $\rm M_{Ceres}$ is the mass of Ceres. If the values of $M_{\rm T,\,d}/10.0{\rm M_{Ceres}}$ and $M_{\rm T,\,d}/0.1{\rm M_{Ceres}}$ are not even integers, they are rounded-up to the nearest even integers. With the known value of $M_{\rm T,\,d}$ and $N_{\rm d}$, the mass is evenly distributed to each debris particle.

If debris particles are formed after a collision, they are evenly distributed in a circle on the plane of impact at a distance of one Hill radius ($R_{\rm Hill}$) from the collision centre of mass according to

$$\boldsymbol{r_{\rm d}} = \boldsymbol{r_{\rm com}} + R_{\rm Hill}\hat{\boldsymbol{r}}_{\rm d}, \tag{2}$$

where $\boldsymbol{r_{\rm d}}$ is the initial position vector of the debris particles, $\boldsymbol{r_{\rm com}}$ is the position vector of the collision centre of mass, and $\hat{\boldsymbol{r}}_{\rm d}$ is the position unit vector for the evenly distributed debris with respect to the collision centre of mass. The velocities of the debris particles are simply assumed to be 5 per cent larger than $V_{\rm esc}$:

$$\boldsymbol{V_{\rm d}} = \boldsymbol{V_{\rm com}} + 1.05 \times V_{\rm esc}\hat{\boldsymbol{r}}_{\rm d}, \tag{3}$$

where $\boldsymbol{V_{\rm d}}$ and $\boldsymbol{V_{\rm com}}$ are the initial velocity vector for the debris and the collision centre of mass velocity vector, respectively.

The accumulated effect of high-energy collisions can lead to the creation of collisional debris in the form of thousands of 'superplanetesimals'. These particles normally get re-accreted by the protoplanets during the simulations, but if, for example, a supercatastrophic collision occurs at the inner edge of our system, then a ring of planetesimals can form, which have exceedingly long dynamical lifetimes. This then causes the simulation run times to increase appreciably. To ameliorate this situation, we have introduced a scheme for removing such a ring of particles when it forms. This is motivated by the fact that the collision time in the ring is normally very short, and collisions between the planetesimals would be highly destructive, such that they would be ground down to dust, which would then be removed by radiation pressure and/or Poynting–Robertson drag. The scheme calculates the collision time and reduces the masses of the planetesimals on that time-scale, until the mass in the ring is negligible and the particles can be removed from the simulation. A more detailed description is given in Appendix A.

2.2 Kepler multiplanet system templates

In this study, we have selected a number of Kepler five-planet multiplanet systems to provide templates for the initial conditions of the simulations, using the following criteria. We are interested in the compact systems, so we have chosen systems in which the known outermost planet has semimajor axis $\leq$0.5 au. We have selected those Kepler systems where all five of the known planets are transiting. For example, the Kepler-122 system is not included due to one of its planets, Kepler-122f, being discovered by transit timing variations (TTVs; Hadden & Lithwick 2014). When we began this project, Kepler-80 was listed as a five-planet system (MacDonald et al. 2016), but more recently it has been confirmed as a six-planet system using deep learning by Shallue & Vanderburg (2018). In spite of this recent announcement, we include this system using the five planets known before 2018. Kepler-296 is a binary system with two stars, Kepler-296A and -296B, that have a projected separation of $\sim$70 au (Barclay et al. 2015). All the five planets are orbiting the same star (Kepler-296A). Given that the outermost planet, Kepler-296Af, orbits at $\sim$0.255 au, which is only $\sim$ 0.36 per cent of the binary stars separation, the binary should have little influence on the dynamic stability and evolution of the planetary system (Wiegert & Holman 1997), and hence we include this system.

As described below, we use the Kepler systems to construct individual mass surface density profiles, which are then used to produce initial conditions for the simulations consisting of 20 protoplanets. We impose selection criteria on these initial conditions that include a requirement that the inter-protoplanet separation is not too small or too large (i.e. $5 \leq K \leq 30$), where K is the inter-protoplanet separation measured in units of the mutual Hill radius. This avoids the evolution being dominated by collisions that occur at very early times before dynamical relaxation of the systems has had an opportunity to arise, or the converse where no collisions happen at all. Finally, we require the maximum value of the initial protoplanet mass to be $M_{\rm p} < 6\,{\rm M}_\oplus$. After applying these criteria, eight systems were selected to be the templates. As listed

Table 1. K-values of the selected Kepler five-planet systems. K_1 to K_4 denote the K-value from the 1st to 4th pair of adjacent planets, respectively, where the 1st pair is the innermost pair and the 4th pair is the outermost pair (penultimate and outermost planets). $\bar{K}$ denotes the arithmetic mean of K for the system. The underlined values are the minimum K values in the system, $K_{\rm min}$. The minimum $K_{\rm min}$ in the table is 7.2, which is greater than the $K_{\rm min} = 7.1$ required to give 100 per cent stable rates in a five-planet system for up to 10^6 yr from Wu et al. (2019).

System	K_1	K_2	K_3	K_4	$\bar{K}$
Kepler-55	23.9	25.6	26.7	10.3	21.6
Kepler-80	41.2	14.5	11.4	7.2	18.6
Kepler-84	24.6	11.6	21.0	13.9	17.8
Kepler-102	22.1	19.4	14.8	18.0	18.6
Kepler-154	34.5	17.4	10.9	16.4	19.8
Kepler-169	29.2	12.4	16.8	45.3	26.0
Kepler-292	15.1	20.0	14.4	14.9	16.1
Kepler-296	17.2	16.2	14.8	18.0	16.5

in Table 1, these are Kepler-55, -80, -84, -102, -154, -169, -292, and -296.

2.3 Surface density profiles from Kepler systems

In order to construct surface density profiles from the chosen Kepler systems, we need to know the semimajor axes and masses of the planets, which are not provided directly by the observations. The semimajor axis is obtained trivially from Kepler's 3rd law:

$$a = \sqrt[3]{\frac{G M_\star}{4\pi^2} P^2}, \tag{4}$$

where P is the measured planetary period and $M_\star$ is the mass of the host star. Numerous suggested relations between the observed planet radius, $R_{\rm p}$, and the planet mass, $M_{\rm p}$, have appeared in the literature. In this study, we adopt the relation suggested by Lissauer et al. (2011a), based on fitting the Earth and Saturn:

$$M_{\rm p} = \left(\frac{R_{\rm p}}{\rm R_\oplus}\right)^{2.06} \rm M_\oplus. \tag{5}$$

We also considered the relation suggested by Wolfgang, Rogers & Ford (2016) (which is the best-fitting relation for the sample of radial velocity (RV) measured transiting sub-Neptunes with $1.5 < R_{\rm p} < 4\,\rm R_\oplus$). As discussed later in Section 3.1, however, we find that obtaining $M_{\rm p}$ from $R_{\rm p}$ using this relation results in some of the selected Kepler systems being themselves dynamically unstable on relatively short time-scales, hence we did not adopt this mass–radius relation in this study.

Once we have $M_{\rm p}$ and $R_{\rm p}$, the internal density, $\rho_{\rm p}$, is given by

$$\rho_{\rm p} = \frac{3M_{\rm p}}{4\pi {R_{\rm p}}^3}. \tag{6}$$

In order to simplify the collision model for a given simulation, we adjusted the $\rho_{\rm p}$ values within each individual system to be the same for different planets, obviating us from having to deal with collision outcomes involving planets with significantly different densities. We did this by constructing a mass-weighted average of the planetary densities as follows:

$$\langle \rho_{\rm p} \rangle = \frac{\sum M_{\rm p}\rho_{\rm p}}{\sum M_{\rm p}}. \tag{7}$$

To find the surface density profile for the original Kepler system, we first define an annulus surrounding each planet. Fig. 1 shows

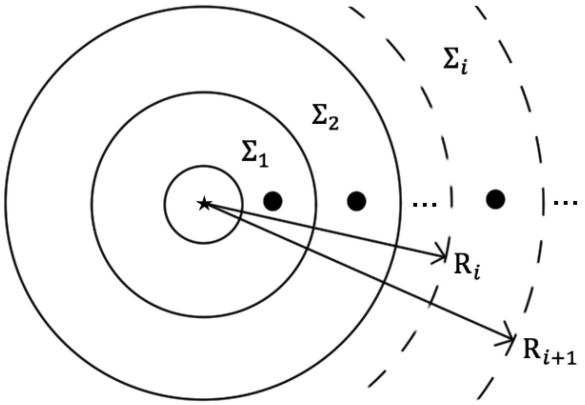

Figure 1. Diagram illustrating method for calculating $\Sigma_{\rm fit}$, the surface density of each of the Kepler templates we have adopted, as described in the text.

an example planetary system and the annuli associated with each planet, where each annulus is defined by its inner and outer radii. For a general planet i, these are denoted as R_i and R_{i+1}. Here, R_i is taken to be the mid-point between the semimajor axis of the planet, a_i, and its inner adjacent planet, a_{i-1}:

$$R_{i,i\neq 1} = \frac{a_i + a_{i-1}}{2}. \tag{8}$$

The innermost boundary is located at

$$R_1 = a_1 - \left(\frac{a_2 - a_1}{2}\right), \tag{9}$$

and when the planetary system has n planets, the outermost boundary, R_{n+1}, is at

$$R_{n+1} = a_n + \left(\frac{a_n - a_{n-1}}{2}\right). \tag{10}$$

The area of the i-th annulus, A_i, is

$$A_i = \pi\left(R_{i+1}^2 - R_i^2\right), \tag{11}$$

and the surface density of the annulus can be calculated using $M_{{\rm p},\,i}$ (the mass of the planet contained in the annulus obtained from equation 5) and A_i from equation (11):

$$\Sigma_i = \frac{M_{\rm p,i}}{A_i}. \tag{12}$$

This gives the surface density at discrete radial locations around each star, and to obtain the surface density as a continuous function we simply fit the five Σ_i values with a smooth function. A fourth-order polynomial can always be found that passes through five real data points, but this approach has not been used here because it often gives negative values of Σ at some locations. Instead, we have fitted the Σ_i using four different model functions, namely

$$\Sigma_{\rm fit}(a) = \begin{cases} c_1 a^{c_2} + c_3 & \text{(13a)} \\ c_1 a^3 + c_2 a^2 + c_3 a + c_4 & \text{(13b)} \\ c_1 \exp(c_2 a) + c_3 & \text{(13c)} \\ c_1 + c_2 \cos(c_4 a) + c_2 \sin(c_4 a), & \text{(13d)} \end{cases}$$

where $\Sigma_{\rm fit}(a)$ is the fitted surface density profile as a function of semimajor axis a; equation (13a) is the power fitting model; (13b) is the polynomial fitting model; (13c) is the exponential fitting model; (13d) is the Fourier series fitting model. The c_i's are the fitting coefficients. The selection criteria for which model to choose are: (1) the model that provides the best least-squares fit among all

models; (2) no negative values between $\Sigma_{\rm fit}(a = R_1)$ and $\Sigma_{\rm fit}(a = R_n)$. Appendix B provides additional details about the coefficients used to obtain $\Sigma_{\rm fit}$ in this study.

2.4 Constructing initial conditions for the simulations

The motivation behind this study is to determine whether or not dynamical instabilities and giant impacts among a large population of protoplanets can lead to final planetary systems that are similar to the compact Kepler multiplanet systems. The initial conditions of the N-body simulations consist of 20 protoplanets that are constructed from the $\Sigma_{\rm fit}$ obtained for each of the Kepler systems.

First, we assume that the semimajor axes of the new protoplanets are distributed following a power law, which is achieved by defining 20 new annuli with appropriate boundaries. The radius of the innermost boundary R_1 and outermost boundary R_{n+1} always remains at the same position as the original Kepler system. The radius of the i-th boundary in between R_1 and R_{n+1} can be calculated by

$$R_{i+1} = f \times R_i, \tag{14}$$

where f is a constant distance ratio and is given by

$$f = \sqrt[n]{\frac{R_{n+1}}{R_1}}. \tag{15}$$

Once R_i are obtained from equation (14), the semimajor axis of the i-th protoplanet, a_i, is set at the mid-point between R_i and R_{i+1}. The mass, $M_{{\rm p},i}$, of the protoplanet in position a_i is calculated according to

$$M_{{\rm p},i} = 2\pi R_i \, (R_{i+1} - R_i) \, \Sigma_{\rm fit}(a_i). \tag{16}$$

Using this process to find the $M_{{\rm p},i}$ values may result in a system with a total mass that differs from the original Kepler system, in which case the mass of each protoplanet is scaled appropriately. Fig. 2 shows the masses of the initial 20 protoplanets with respect to their semimajor axis for each system template. We also assumed that the density of the protoplanets is $\rho_{\rm p} = \langle \rho_{\rm p} \rangle$ throughout the whole system. With the new value of $\rho_{\rm p}$ and $M_{\rm p}$, the planetary radii, $R_{\rm p}$, adopted in the simulations can be obtained from equation (6).

The initial eccentricities, e, inclinations, I, arguments of pericentre, ω, longitudes of ascending node, Ω, and mean anomalies, M, also need to be defined when setting the initial conditions of the simulations. The values of e and I are uniformly distributed within a range $0 \leq e \leq e_{\rm max}$ and $0 \leq I \leq I_{\rm max}$, where $e_{\rm max}$ and $I_{\rm max}$ are defined below. The values of ω, Ω, and M are distributed uniformly in the range $0 \leq (\omega, \Omega, M) \leq 2\pi$.

Two sets of $e_{\rm max}$ and $I_{\rm max}$ values are used here to investigate the effect of the initial eccentricities and inclinations. The first (higher initial value) set has $e_{\rm max} = 0.02$ and $I_{\rm max} = 0.01$ rad, while the second (lower initial value) set has $e_{\rm max} = 0.002$ and $I_{\rm max} = 0.001$ rad. In each $e_{\rm max}$–$I_{\rm max}$ set, 10 simulations were run, with different random number seeds being used to generate the values of ω, Ω, and M. Hereafter, the 'higher set' refers to the runs with ($e_{\rm max}$, $I_{\rm max}$) = (0.02, 0.01), and the 'lower set' refers to the runs with ($e_{\rm max}$, $I_{\rm max}$) = (0.002, 0.001). Each higher and lower set was run using both perfect and imperfect collision models using the `MERCURY` and `SyMBA` N-body codes, respectively. Hence, there are 40 simulations for each Kepler system template.

The central bodies of each system have their masses and radii taken from the Kepler data. Each simulation runs for 10^7 yr. The time-steps used in the simulations are set to be 1/20th of the shortest orbital period (Duncan et al. 1998).

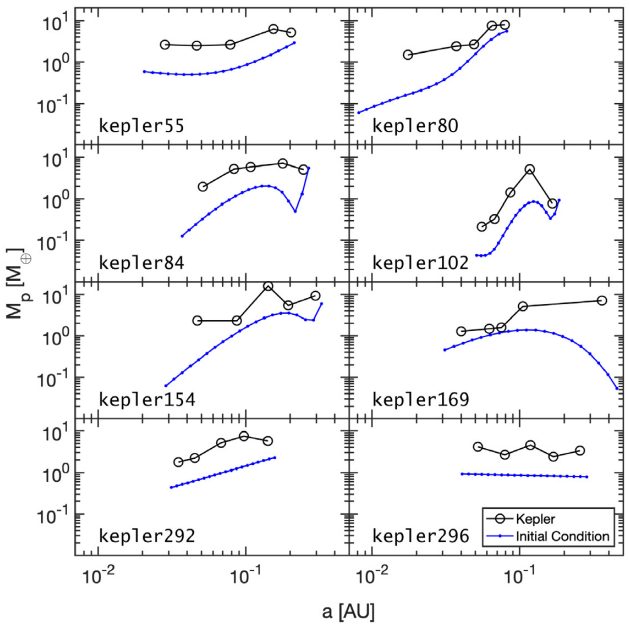

Figure 2. $M_{\rm p}$ versus a for all eight Kepler templates. Initial masses of the 20 protoplanets are marked in blue dots, and the original Kepler planet masses are marked in black circles.

As discussed above in Section 2.2, one of the criteria used to constrain our initial conditions is that the mutual separation between neighbouring protoplanets must satisfy $5 \leq K \leq 30$, where K is the inter-protoplanet separation measured in units of the mutual Hill radius. The mutual Hill radius for a pair of adjacent planets is defined by

$$R_{{\rm H},i} = \frac{a_i + a_{i+1}}{2} \left(\frac{M_{{\rm p},i} + M_{{\rm p},i+1}}{3 M_\star} \right)^{1/3}. \tag{17}$$

The dimensionless number K can then be expressed as

$$K_i = \frac{a_{i+1} - a_i}{R_{Hi}}, \tag{18}$$

where K_i is the K-value for the i-th pair of adjacent planets in the system.

For a Kepler planetary system, applying the value of a obtained from equation (4), $M_{\rm p}$ from equation (5), and $M_\star$ from the Kepler data, K can be directly calculated by equation (18). For the selected Kepler planetary systems in this study (see Section 2.2), the K_i values for each planet pair and mean K value of each system, $\bar{K}$, are listed in Table 1. The overall mean K value across all selected systems has the value $\langle \bar{K} \rangle \approx 19.4$. This value is about the same as the typical average K value for Kepler multiplanetary systems (see Section 1).

Finally, we comment that the initial conditions of the simulations presented in this paper represent the state of the system after substantial evolution has already taken place, and once the gaseous protoplanetary disc has been dispersed. For discussion of possible scenarios leading to these initial conditions, involving the accretion of planetesimals, boulders, and/or pebbles onto planetary embryos embedded within the gas disc, we refer the reader to the following papers that present the results of N-body simulations of these earlier epochs of planet formation (Coleman & Nelson 2014, 2016; Izidoro et al. 2019; Lambrechts et al. 2019).

3 RESULTS

3.1 Stability of the original Kepler multiplanet systems

Before embarking on a study of the formation of the Kepler systems considered in this paper, we begin by considering the dynamical stability of the observed systems themselves. This acts as a consistency check on the mass–radius relation used to construct the initial conditions for the formation simulations, given by equation (5) (Lissauer et al. 2011a). Since the first multiplanet systems discovered by Kepler were confirmed, a number of mass–radius relations have been suggested. For example, Wu & Lithwick (2013) suggested $M_{\rm p} = 3\,{\rm M}_{\oplus}(R_{\rm p}/{\rm R}_{\oplus})$, Weiss & Marcy (2014) suggested $M_{\rm p} = 2.69\,{\rm M}_{\oplus}(R_{\rm p}/{\rm R}_{\oplus})^{0.93}$, and Wolfgang et al. (2016) suggested $M_{\rm p} = 2.7\,{\rm M}_{\oplus}(R_{\rm p}/{\rm R}_{\oplus})^{1.3}$. Clearly, given that the masses obtained from each of these relations vary for specific values of the planetary radii, stability of the confirmed system is not guaranteed to hold under all these relations. Checking the stability hence provides some constraint on the mass–radius relation that applies.

We carried out a stability check for all Kepler five-planet systems, including those that do not obey the selection criteria mentioned in Section 2.2, comparing the relation suggested by Wolfgang et al. (2016) and that provided by Lissauer et al. (2011a). We performed *N*-body simulations using `Mercury`, and adopted initial conditions that assumed that the system planets are initially on circular and coplanar orbits ($e = 0$ and $I = 0$ for all planets). The initial values of the mean anomalies of the planets were assigned randomly, and 10 different realizations were run for each system. We found that the relation from Lissauer et al. (2011a) provides stable systems for all five-planet systems over a 10 Myr run time, while the mass–radius relation provided by Wolfgang et al. (2016) fails to produce stable systems for some Kepler systems over the same time-scale [e.g. the systems Kepler-32 and -33, which were validated by Lissauer et al. (2011a)]. For this reason, the relation provided by Lissauer et al. (2011a) is the one we used to construct the initial conditions for the 20-protoplanet simulations described in the following sections.

3.2 Results of the formation simulations

To recap, two sets of *N*-body simulations were performed for each Kepler template, one assuming perfect accretion using a simple hit-and-stick model, and the other adopting the imperfect accretion algorithm of Leinhardt & Stewart (2012). For each Kepler template, we considered two initial distributions of the eccentricities and inclinations, a 'high set' and a 'low set', and for each of these we computed 10 different realizations of the initial conditions by varying the random number seeds used to create the initial conditions. Hence, we ran 40 *N*-body simulations for 10 Myr for each Kepler template.

We begin our discussion of the results by first considering how the simulation outcomes considered as a whole vary when considering the perfect and imperfect accretion prescriptions. We then look at the simulations in more detail by considering how the outcomes vary between the different Kepler templates, focusing on the resulting planet masses, orbital elements, period ratios, *K*-values, and system architectures that emerge from the simulations.

3.2.1 Comparison between perfect and imperfect accretion across all runs

The distributions of the semimajor axes, eccentricities, inclinations, and masses are shown in the histograms and cumulative distribution functions (CDFs) in Fig. 3. Later in the paper, we discuss the mutual separations between pairs of planets, and the *K*-values are shown in Fig. 11. By-eye inspection suggests that the distributions are in good agreement when comparing the perfect and imperfect accretion models, and applying the Kolmogorov–Smirnov test (K–S test) yields *p*-values of 0.148 for the semimajor axis distributions, 0.100 for the eccentricities, 0.079 for the inclinations, and 0.234 for the masses. Hence, the null hypothesis that the data plotted in Fig. 3 for the perfect and imperfect collision simulations are drawn from the same underlying distribution cannot be rejected with a $>$ 95 per cent confidence level.

Agreement between the perfect and imperfect accretion runs can also be seen when looking at individual system templates. For example, Fig. 4 shows the CDFs for the same parameters shown in Fig. 3, but only for the `Kepler55` system template, and again it can be seen that the distributions are very similar. Here the K–S test yields *p*-values of 0.995 for the semimajor axis distributions, 0.832 for the eccentricities, 0.166 for the inclinations, and 0.734 for the masses.

In summary, based on the global properties of the final planetary systems that are formed, we can conclude that the differences produced by the perfect and imperfect accretion prescriptions are small, and do not have a statistically significant influence on the outcomes of the simulations.

3.2.2 Instabilities and multiplicities

All simulations resulted in dynamical instabilities that led to mutual scattering and giant impacts. Fig. 5 shows the distributions of the multiplicities of all final planetary systems. The maximum number of planets remaining after 10 Myr was 12 and the minimum was 3. No single or double planet systems were formed. Having four or five planets remain in the system is the most common outcome. Our multiplicity distribution appears to agree with the distribution obtained by Hansen & Murray (2013), where they also obtain a minimum multiplicity of 3, and a peak in the multiplicity distribution at four or five planets. The mean value of the number of planets obtained in the imperfect collision simulation is $\langle N_{\rm I}\rangle = 5.21$, and for perfect collisions it is $\langle N_{\rm P}\rangle = 5.06$. For the higher initial value set $\langle N_{\rm H}\rangle = 5.05$, and for the lower initial value set $\langle N_{\rm L}\rangle = 5.22$. It is noteworthy how close these values are to 5, given that our template systems all contain five planets, indicating that the initial conditions constructed from the templates are able to reproduce the desired multiplicity on average. In a recent analysis of the Kepler data, Zhu et al. (2018) concluded that the mean number of super-Earths in compact systems around solar-type stars is approximately 3, with the fraction of stars hosting planetary systems being approximately 0.3. This suggests that the five-planet systems we have chosen for this study may not be representative of the Kepler planets as a whole, even if we allow for the fact that the Kepler systems contain unseen planets by virtue of them being on orbits that are inclined to the line of sight.

The K–S test applied to the CDFs derived from the data in Fig. 5 gives a *p*-value of 0.997 for the perfect and imperfect collision models, and 0.999 for the runs with the higher and lower initial eccentricity/inclination values. The small difference between $\langle N_{\rm I}\rangle$ and $\langle N_{\rm P}\rangle$, together with the large *p*-value, shows that our runs are in accord with the conclusions reached by Mustill et al. (2018), namely that assuming either perfect or imperfect collisions has little impact on the final multiplicities. The similar values for $N_{\rm H}$ and $N_{\rm L}$ show

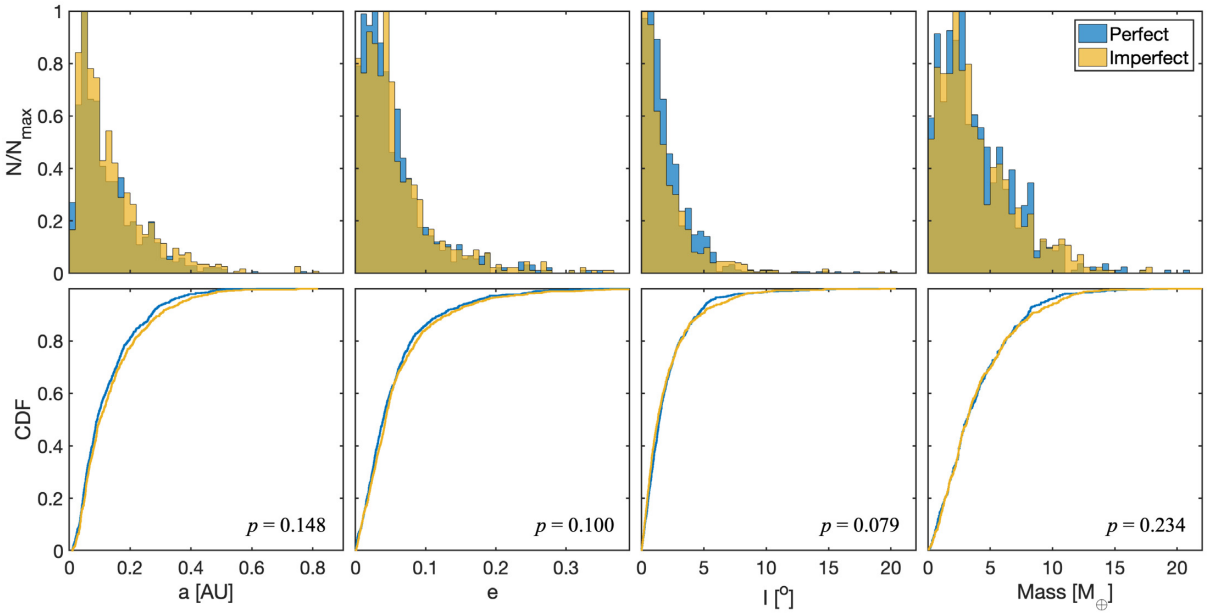

Figure 3. The normalized distributions (top panel) and the cumulative distribution functions (CDFs, bottom panel) of the semimajor axes, eccentricities, inclinations, and planet masses of the planets obtained in all simulations. Perfect collision simulations are shown in blue, and imperfect collision simulations are shown in yellow.

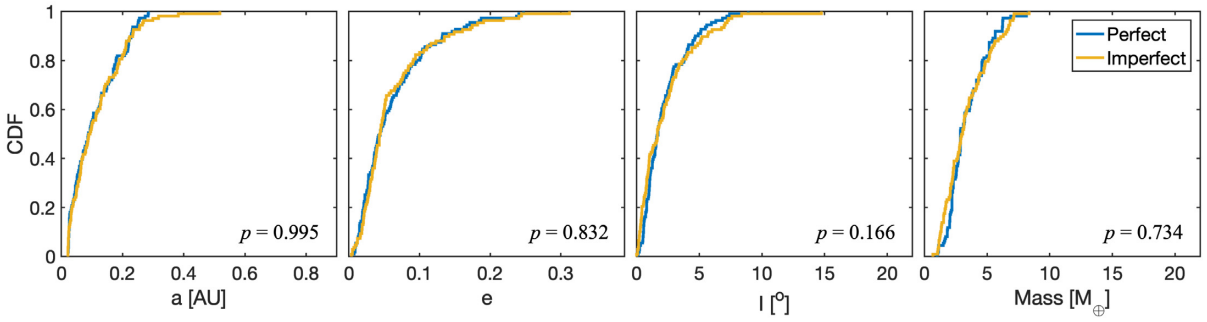

Figure 4. Cumulative distributions, from all simulations of the `Kepler55` template, of the same four parameters listed in Fig. 3. They are (in order from left to right) a, e, I, and M_p. The blue and yellow lines are for the perfect collision and imperfect collision simulations, respectively.

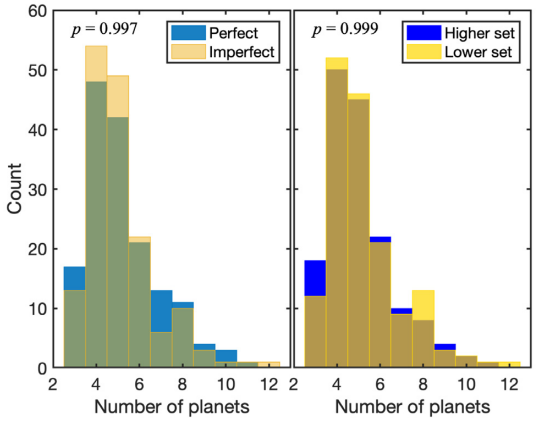

Figure 5. Multiplicity distributions from all simulations. The left-hand panel compares the distributions obtained in the perfect and imperfect collision simulations. The right-hand panel compares the distributions obtained in the high and low initial eccentricity/inclination simulations (see Section 2.4 for the definitions of these simulation sets).

that the initial value of e and I also has a limited impact on the final multiplicities, at least for the range of values adopted here.

Fig. 6 shows the CDF for the occurrence times of all giant impact events detected during the imperfect collision simulations. More than 90 per cent of the giant impacts happened before 1 Myr (the white area in the figure), and 50 per cent of the impacts occurred within 10^4 yr. Given that the planetary systems are centred around $a \sim 0.1$ au, this latter figure corresponds to $\sim 3 \times 10^5$ dynamical times, indicating that the initial conditions do not result in excessively short accretion times. Instead, the systems have time to undergo substantial dynamical relaxation during the epoch of accretion. Furthermore, the fact that only 10 per cent of the collisions occur after 1 Myr indicates that our run times of 10 Myr are long enough to have formed long-term stable systems in most cases. However, the fact that some collisions are occurring at late times also indicates that some of our final planetary systems would have evolved further if the integrations had been extended. Finally, we note that with 90 per cent of the collisions occurring in the simulations within 1 Myr, this implies that if the protoplanets we consider in the initial conditions were formed within the lifetime of the

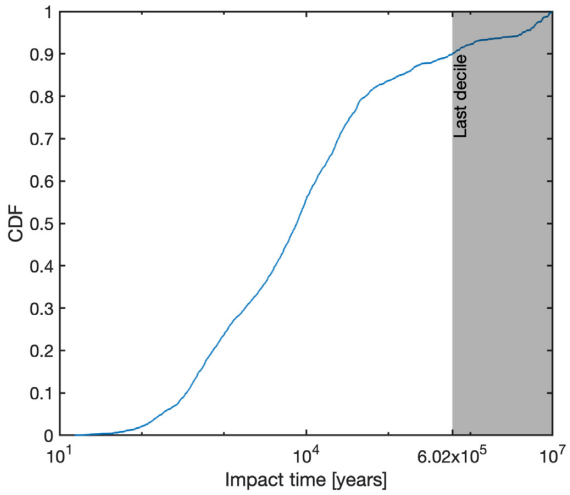

Figure 6. Cumulative distribution of all the giant impact events with respect to time during the imperfect collision simulations. The grey area denotes the latest 10 per cent of the collisions.

gaseous protoplanetary discs, then substantial collisional evolution would have likely occurred while the gas was still present as disc lifetimes are typically 3 Myr (Haisch, Lada & Lada 2001). Ogihara, Morbidelli & Guillot (2015) have shown that under such conditions the effects of migration cannot be ignored and strongly influence the architectures of the resulting systems.

3.2.3 *Eccentricities, inclinations, and masses*

Table 2 lists the mean values of e, I, and the K-values for each subset of runs associated with each of the Kepler templates. Hence, the averaging has been performed over the final outcomes of the 10 simulations associated with perfect/imperfect accretion and high and low initial eccentricities/inclinations. While there is some variation of the mean eccentricities and inclinations when comparing the different initial eccentricities/inclinations and the accretion prescription (particularly for `Kepler80`), the largest variation is observed when comparing the different Kepler templates. For example, the `Kepler55` runs all give $\langle e \rangle \sim 0.06$, whereas the `Kepler296` runs give higher values distributed around $\langle e \rangle \sim 0.09$.

The top and middle panels of Fig. 7 show the values of e and I with respect to semimajor axis a from four of the simulation templates performed with the imperfect collision model (see Fig. C1 in Appendix C for the results of the other four templates that adopt imperfect collisions, and Figs C3 and C5 for all eight templates that use the perfect collision model). The plots show that the final distributions arising from the higher set (blue triangles) and the lower set (yellow diamonds) are very similar. This is not surprising as the initial eccentricities and inclinations in all of these runs are considerably smaller than the mean values at the ends of the simulations. Hence, the final values are determined by planet–planet scattering and collisional damping, and little memory is retained of the original eccentricity and inclination values. This would not be the case if the initial eccentricities and inclinations had been comparable to or larger than the values obtained from dynamical relaxation (Matsumoto & Kokubo 2017). It is common to see that e and I have relatively high values near the inner and outer edges of the systems, perhaps best illustrated by the `Kepler102` and `Kepler169` templates. This feature was already noted by Hansen & Murray (2013) in their study of *in situ* formation of super-Earths, and arises because bodies at the edge of the initial annulus of protoplanets are scattered outwards and do not experience collisions that tend to damp the eccentricities and inclinations.

The bottom panels of Fig. 7 show the final planet masses versus their semimajor axes. A striking feature of these plots is how the simulated systems (denoted by blue triangles for higher set runs, and yellow diamonds for lower set runs) generally match the observed Kepler systems (denoted by black circles joined by solid lines). Hence, based on this comparison alone, it is reasonable to conclude that the initial conditions and formation histories that we simulate here might be reasonable approximations to those that applied to the actual Kepler systems we have used as templates. The exception is `Kepler169`, where the outer regions of these simulations failed to generate significant collisional growth because the initial masses of the protoplanets there, generated by the method mentioned in Section 2.4, were too small (giving initial K-values >15), leading to instability times longer than the 10 Myr simulation run times.

In view of this, we extended the run times of the `Kepler169` template simulations to 100 Myr, using the perfect accretion routine (see Fig. C7 in Appendix C for the comparison). As expected, the outer regions of the systems experienced increased growth and provided better agreement with the original Kepler masses. This suggests that a better strategy for future work would be to run simulations for a set number of orbits measured at the outer edges of the systems, instead of a fixed number of years as was done in this work.

Although the final planet masses in the simulations match their Kepler templates on average, it is worth noting that when we consider the CDF of planet masses later in this paper, and compare it with that obtained from the original Kepler template systems (see Fig. 21), the agreement is not good because the simulations produce a range of planetary systems, some of which have higher multiplicity than 5 and hence contain planets with relatively low masses.

As with the eccentricities and inclination distributions discussed above, there are no systematic differences in the final planetary masses when comparing the high and low initial eccentricity/inclination subsets of runs.

The high values of e and I at the edges of the system due to planets being scattered but experiencing fewer collisions there, discussed above and noted by Hansen & Murray (2013), can also be seen in Fig. 8, which shows the final planets from all runs in the a–e plane (top panel), a–I plane (middle panel), and a–$M_{\rm p}$ plane (bottom panel). We also see from the lower panel that higher mass planets occupy the centre of the a–$M_{\rm p}$ plane, where collisional growth occurs more frequently, with lower mass planets being present at the edges of the annuli where collisions occur less frequently. Fig. 9 shows that e and I are strongly correlated, as expected for systems that have undergone dynamical relaxation.

3.2.4 *Period ratios and* K*-values*

Fig. 10 shows that the perfect and imperfect accretion simulations provide similar cumulative distributions of the period ratios between neighbouring planet pairs. We can compare these with the distribution of period ratios for the actual Kepler multiplanet systems. In Section 7.2 below, we also compare the period ratios obtained from the simulations when they are synthetically observed with the Kepler data, but here we focus on the intrinsic period ratios. For period ratios smaller than 4:3, we see that the Kepler data show an excess compared to the simulations. A K–S test performed on a subset of period ratios between 5:4 and 4:3 gives

Table 2. Mean values of e, I, and K-values from the different simulation subsets from all eight Kepler templates. The numbers in parentheses are the standard deviations about the respective means.

System Elements	Kepler System	Imperfect <Higher>	Imperfect <Lower>	Perfect <Higher>	Perfect <Lower>	All <Higher>	All <Lower>	All Imperfect	All Perfect	All Sets
$\langle e \rangle$	55	$6.32_{(5.71)}$	$6.27_{(5.50)}$	$6.03_{(4.46)}$	$6.34_{(5.97)}$	6.18	6.31	6.30	6.19	6.24
($\times 10^{-2}$)	80	$3.21_{(4.47)}$	$5.09_{(5.50)}$	$1.85_{(2.25)}$	$1.88_{(1.90)}$	2.53	3.49	4.15	1.87	3.01
–	84	$7.02_{(4.86)}$	$5.20_{(4.56)}$	$6.32_{(6.14)}$	$5.91_{(4.39)}$	6.67	5.56	6.11	6.12	6.11
–	102	$5.55_{(6.64)}$	$3.74_{(2.81)}$	$5.64_{(4.46)}$	$6.27_{(7.30)}$	5.60	5.01	4.65	5.96	5.30
–	154	$8.46_{(6.65)}$	$5.25_{(5.68)}$	$7.23_{(7.02)}$	$7.12_{(7.17)}$	7.85	6.19	6.86	7.18	7.02
–	169	$4.42_{(2.72)}$	$5.49_{(6.22)}$	$4.68_{(4.06)}$	$4.70_{(6.92)}$	4.55	5.10	4.96	4.69	4.82
–	292	$5.43_{(3.08)}$	$5.04_{(4.00)}$	$6.65_{(5.20)}$	$5.72_{(3.60)}$	6.04	5.38	5.24	6.19	5.71
–	296	$10.28_{(9.86)}$	$11.40_{(11.05)}$	$7.60_{(5.72)}$	$9.90_{(6.64)}$	8.94	10.65	10.84	8.75	9.80
$\langle I \rangle$	55	$4.34_{(4.85)}$	$3.74_{(2.90)}$	$4.31_{(3.55)}$	$3.47_{(2.61)}$	4.33	3.61	4.04	3.89	3.97
($\times 10^{-2}$)	80	$1.18_{(1.20)}$	$1.67_{(2.45)}$	$2.72_{(3.89)}$	$1.41_{(1.96)}$	1.95	1.54	1.43	2.06	1.74
[rad]	84	$3.38_{(2.86)}$	$3.63_{(3.51)}$	$3.18_{(3.61)}$	$3.97_{(4.39)}$	3.28	3.80	3.51	3.58	3.54
–	102	$2.52_{(3.03)}$	$2.38_{(2.45)}$	$3.65_{(4.30)}$	$3.93_{(3.64)}$	3.08	3.15	2.45	3.79	3.12
–	154	$5.00_{(5.68)}$	$5.62_{(3.82)}$	$4.94_{(6.94)}$	$5.38_{(6.33)}$	4.97	5.50	5.31	5.16	5.23
–	169	$2.38_{(1.92)}$	$3.48_{(3.41)}$	$3.42_{(2.32)}$	$3.00_{(2.30)}$	2.90	3.24	2.93	3.21	3.07
–	292	$4.19_{(2.95)}$	$2.94_{(2.66)}$	$2.33_{(1.87)}$	$2.87_{(2.42)}$	3.26	2.90	3.56	2.60	3.08
–	296	$5.90_{(3.56)}$	$7.89_{(7.91)}$	$5.32_{(2.76)}$	$5.90_{(4.67)}$	5.61	6.90	6.89	5.61	6.25
$\langle K \rangle$	55	$21.1_{(6.43)}$	$21.2_{(6.91)}$	$22.6_{(6.25)}$	$20.9_{(7.17)}$	21.8	21.1	21.2	21.7	21.4
–	80	$21.5_{(11.37)}$	$22.8_{(11.09)}$	$20.6_{(10.40)}$	$19.0_{(10.40)}$	21.0	20.9	22.2	19.8	21.0
–	84	$21.2_{(4.80)}$	$19.2_{(5.42)}$	$20.8_{(4.79)}$	$19.8_{(4.81)}$	21.0	19.5	20.2	20.3	20.3
–	102	$21.4_{(6.54)}$	$19.1_{(6.01)}$	$20.6_{(5.97)}$	$21.9_{(4.59)}$	21.0	20.4	20.3	21.1	20.7
–	154	$20.7_{(6.82)}$	$19.0_{(6.46)}$	$20.4_{(7.43)}$	$18.7_{(8.16)}$	20.6	18.9	19.9	19.6	19.7
–	169	$21.1_{(6.23)}$	$22.5_{(7.61)}$	$22.2_{(6.74)}$	$21.9_{(9.70)}$	21.6	22.2	21.8	22.0	21.9
–	292	$19.5_{(3.87)}$	$18.5_{(4.23)}$	$18.7_{(4.40)}$	$17.3_{(5.28)}$	19.1	17.9	19.0	18.0	18.5
–	296	$24.3_{(7.47)}$	$22.9_{(9.15)}$	$22.4_{(5.69)}$	$21.4_{(4.37)}$	23.4	22.2	23.6	21.9	22.8

p-values of 1.69×10^{-4} and 0.029 when comparing the Kepler data with the perfect and imperfect collision simulations, respectively, demonstrating that the distributions are different. Hence, some process occurred during the formation of at least some Kepler systems that allowed the survival of more compact architectures, which are none the less non-resonant. Dynamical relaxation and collisional evolution in the absence of any dissipative process clearly result in such closely separated planet pairs being destabilized, suggesting that those Kepler systems with particularly compact configurations formed in a dissipative environment and did not undergo dynamical instability in spite of the close proximities of the planets. One such system not considered here that displays this property is Kepler-11 (Mahajan & Wu 2014).

The full Kepler data set, without any limits in period ratio being applied, clearly contains too many planet pairs with large period ratios compared to the simulation intrinsic outcomes, and a K–S test comparing the data and simulations results in p-values <0.05. Again, such system architectures do not naturally arise from a formation scenario in which even a wide annulus of protoplanets undergoes dynamical instability and collisional growth, since this mode of evolution results in neighbouring planets being separated by $\sim$20 mutual Hill radii (see the discussion below). Instead, additional processes would need to be invoked, which either cause the initial distribution of protoplanets to have a more complex structure involving concentrations around particular orbital radii, or which involve orbital migration because formation occurred in the presence of either a gas or planetesimal disc. Considering planet pairs in the Kepler data with a maximum period ratio of 3:1 results in much better agreement between the observational data and simulations, with p-values of 0.078 and 0.120 for perfect and imperfect collisions, respectively. However, we also note here that the synthetically observed systems, described in Section 7.2, provide a distribution of period ratios that is quite different to that obtained from the simulations directly, due to the fact that mutual inclinations between the planets lead to some planets not being detected during the observations. This has the effect of increasing the numbers of systems with large period ratios.

One feature within the Kepler multiplanet systems that the simulations do not reproduce particularly well is the known peaks in occurrence rates of planet pairs just outside of the 3:2 and 2:1 resonances (seen in particular as a flattening and then rise in the CDF at around period ratio 2:1 in Fig. 10). The cumulative distribution for the simulation data shows a very modest inflection around the 2:1 resonance, but it is not as pronounced as in the Kepler data, and is not statistically significant. It is noteworthy that Petrovich, Malhotra & Tremaine (2013) were able to reproduce the resonance features using three-body integrations that resulted in final systems of two planets for planet masses $20 \leq M_{\rm p} \leq 100$ M$_\oplus$. The end states of our simulations always have more than two planets, and the final planet masses are typically <10 M$_\oplus$. These properties likely serve to reduce the prominence of features in the period ratio distribution near first-order mean motion resonances, and leave open the question of what dynamical processes have given rise to the near-resonance features in the period ratio distributions of the Kepler planets.

The distributions of the K-values from all our simulations can be seen in Fig. 11. Both collision models result in similar distributions, with a p-value of 0.54, with 50 per cent of systems having $10 \leq K \leq 20$, and the maximum value of K being $\sim$50. Although not obvious in the plot, the number of planets with $K < 10$ decreases to zero and then rises again close to $K = 0$, with these latter planets surviving because they are protected by a 1:1 resonance. Wu et al. (2019) have

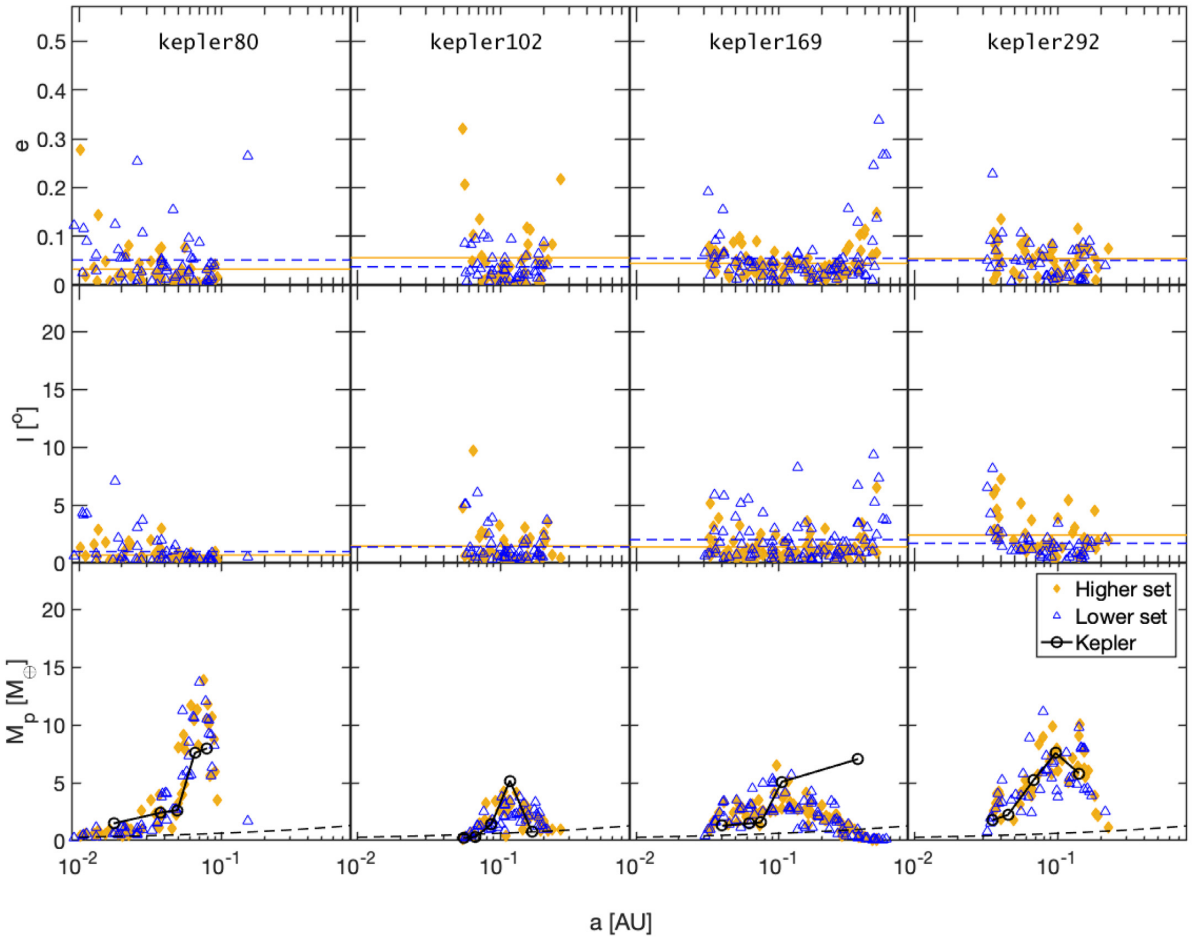

Figure 7. All imperfect collision simulation results from (from left to right) `Kepler80`, `102`, `169`, and `292` templates. The scatter plots show the eccentricities (top panel), inclinations (middle panel), and planet masses (bottom panel) with respect to their semimajor axis. The orange-diamond data are from the higher initial eccentricity set, and the blue-triangle data are from the lower initial eccentricity set. The horizontal lines in each subplot show the mean values of the data in their respective colour (also plotted as solid lines for the higher initial eccentricity set and dashed lines for the lower initial eccentricity set). The black circles in the bottom panel denote the masses and semimajor axes of the observed Kepler planets. The black dashed lines indicate the detection limit applied when undertaking the synthetic transit observations described in Section 7.1.

presented similar simulation results on this feature in the *K*-value distribution and its relation to the 1:1 resonance (period ratio $<$ 1.05), and we discuss these co-orbital systems further in the next section. Fig. 12 shows the value of *K* for each planet pair using the same four Kepler templates shown in Fig. 7 (see Fig. C2 in Appendix C for the results of the other four templates that adopt imperfect collisions, and Figs C4 and C6 for all eight templates that use the perfect collision model). The distributions of the *K*-values are similar, independent of whether we consider the high- or low-eccentricity/inclination set. And they also show similar *K*-values compared to the original Kepler systems (shown by the black circles joined by lines), based on the adopted mass–radius relation, although again the `Kepler169` system is an exception (see Fig. C8 in Appendix C for a comparison to systems that were evolved for 100 Myr instead of 10 Myr).

4 CO-ORBITAL PLANET PAIRS

In Section 3.2.4, we stated that a small number of planets have very small *K*-values, and these are shown in the Fig. 11. Further investigation has shown that these planets have been captured into 1:1 co-orbital resonances, and these co-orbital planets make up about 1 per cent (4 out of 320 simulations) of the total number of planet pairs.

4.1 Stability

In spite of the very small *K*-values, the 1:1 resonance protects co-orbital planet pairs from instability. In general, both stable tadpole orbits, which involve libration around the L4/L5 points, and horseshoe orbits are permitted (Dermott & Murray 1981a, b), and we see examples of both of these orbit types in the simulations. As the simulation run times are 10 Myr, and the co-orbital pairs are found to form early in some simulations, we find tadpole and horseshoe orbits that are stable for 9.5×10^6 yr. This is in spite of the co-orbital pairs being in systems of high multiplicity, where the resonance configuration is subject to external perturbations. Previous studies have shown that co-orbital planet pairs can be stable for up to 10^9 yr (Tabachnik & Evans 2000). Fig. 13 shows an example of the semimajor axis versus time during the last 10 yr of one simulation (the left-hand panel) and the corresponding orbital trajectory of the 1:1 resonance planet pair from the same model in a

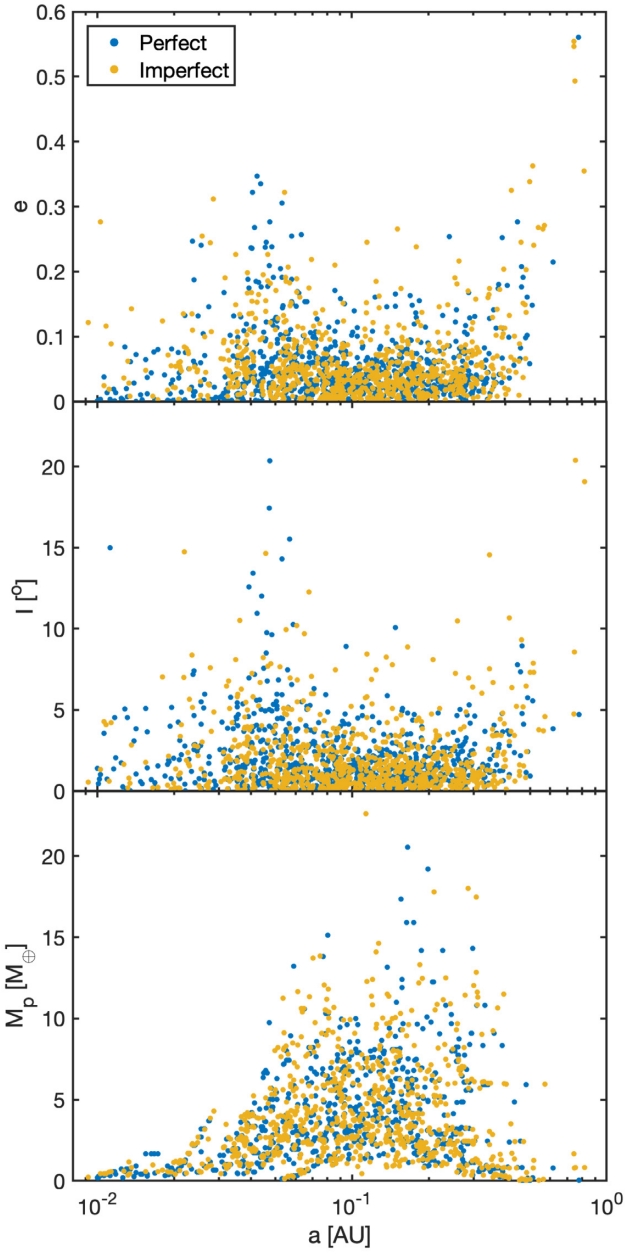

Figure 8. Scatter plots comparing e, I, and M_p as a function of a arising from perfect (blue points) and imperfect (yellow points) collision simulations.

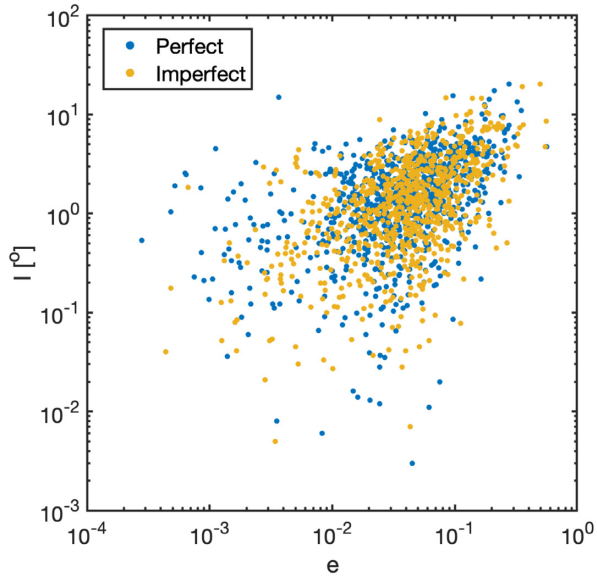

Figure 9. Scatter plot showing correlation between e and I from all runs. Perfect collision results are shown by blue points, and imperfect collision results are shown by yellow points.

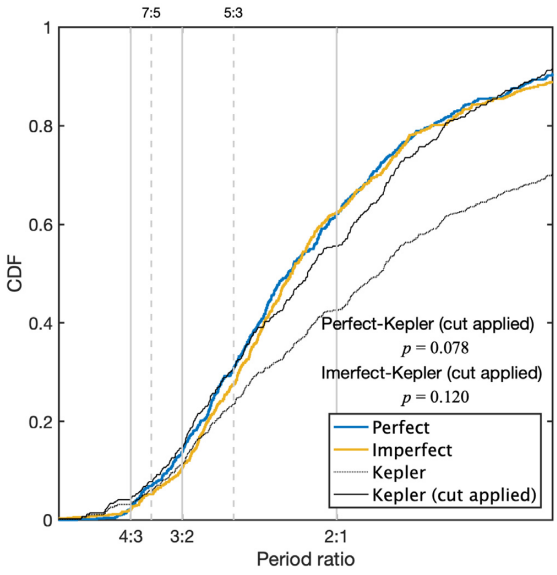

Figure 10. CDFs of the period ratios of all adjacent planet pairs. The blue and yellow lines correspond to the perfect and imperfect collision models, respectively. The black dotted line includes all the original Kepler planet pairs. The solid black line shows the original Kepler planet pairs with a cut-off for a period ratio >3.

frame that co-rotates with one of the planets (the right-hand panel). From the semimajor axis plot, we can see the two planets undergo a periodic exchange of radial location, and the co-rotating plot shows that the orbit is a tadpole orbit.

In other simulations that produce 1:1 resonant planet pairs, we see similar characteristics in the semimajor axis evolution. Although it is generally expected that horseshoe orbits are not as stable as tadpole orbits (Dermott & Murray 1981b), the planet pairs in horseshoe orbits produced in the simulations are found to be stable over the runs times we consider. The maximum value of the period ratio among all the co-orbital pairs is ∼1.05:1, in agreement with the simulations by Wu et al. (2019), which show that period ratios in the range 1.05–1.1 are unstable (independent of whether or not the system has two planets or a higher multiplicity).

4.2 Formation

All the co-orbital planet pairs form fairly early in our simulations (within a few thousand years). Fig. 14 demonstrates the formation of a co-orbital pair by a two-body collision event in the perfect collision model. The top panel shows the evolution of the semimajor axis during the first 2000 yr of the simulation. We can see the collision happened around 1200 yr (black dashed line). The three bodies involved in the encounter are marked by blue, green, and purple lines (labelled as planet-b, planet-g, and planet-p, respectively, from now on). In this encounter, planet-g and planet-p are the surviving

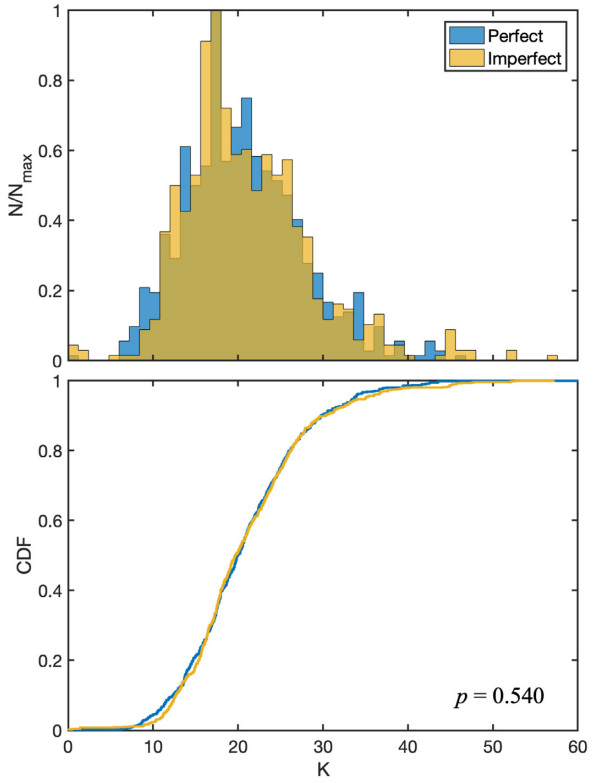

Figure 11. The normalized distributions (top panel) and the cumulative distributions (bottom panel) of the *K*-value of the planet pairs obtained in all our simulations. Perfect collision simulations are shown in blue, and imperfect collision simulations are shown in yellow.

planets and they form a co-orbital tadpole orbit. The second panel of the figure shows the change of mass of the bodies during the evolution. We can see that planet-b collided with planet-p during the encounter, and the resulting body ended up with the appropriate energy and angular momentum so that it could settle into a co-orbital configuration with planet-g. The figure also shows the eccentricity and inclination evolution in the bottom two panels. The eccentricity evolution shows the angular momentum and energy exchange (Funk et al. 2011; Funk, Dvorak & Schwarz 2013) between planet-g and planet-p. The fluctuations of these two orbital elements are seen to be reduced after the encounter compared to before it, because of the collision and formation of the co-orbital pair. The two co-orbital planets are mutually inclined by approximately 2°, and hence it cannot be guaranteed that both the planets would be detected in a photometric survey searching for transiting planets.

It is clear that formation of a co-orbital planet pair, involving two planets that were initially well separated in orbital radius, requires energy and angular momentum loss from one of the planets. Within our simulations, there are three possible ways to achieve this energy loss: (1) an inelastic collision between two bodies resulting in the composite body having the appropriate energy and angular momentum to form a co-orbital pair with a third planet; (2) interaction with collision debris (in the form of multiple planetesimals) formed from an earlier collision, leading to the requisite change in energy and angular momentum by the members of the co-orbital pair; (3) a three-body encounter in which energy and angular momentum from at least one planet in the co-orbital pair are given to a third body. The case illustrated in Fig. 14 corresponds to the first of these formation scenarios. Neither the interaction with debris nor the three-body encounter formation mechanisms were observed in the simulations, although simulations using the perfect and imperfect accretion routines both resulted in the formation of co-orbital pairs. All systems that formed co-orbital pairs did so early in the simulations, when the space density of planets and the probability of capture due to kinetic energy loss of the colliding planets were at their highest.

4.3 Resonance-induced TTV

The co-orbital planet pair (planet-p and planet-g) shown in Fig. 14 survived to the end of the 10 Myr evolution. The final mutual inclination of this planet pair is $\sim 2^o$, which makes it unlikely that both the planets would be detected directly during a transit survey. On the other hand, this type of 1:1 resonance pair would induce TTVs on each other, which might provide a signal indicating the presence of the other non-transiting co-orbital planet.

Fig. 15 demonstrates the TTV signal expected for planet-g during a 10 yr period after the end of the simulation. Here, we have calculated the mean orbital period of planet-g over this 10 yr period ($P_g \approx 9.9872$ d), and have then computed the Observed−Calculated ($O - C$) times for the transits of planet-g. The amplitude of the TTV signal reaches ± 0.9639 d, and the maximum difference between adjacent periods is $\sim$15 min. If it was possible to pick up the transit signal of planet-g and confirm it as a planet within a transit survey, then the TTV signal would provide strong evidence of the presence of the other planet (e.g. planet-p in this case). However, we note that such a strong TTV signal might also provide a barrier to detecting co-orbital planets in the automated pipelines of transit surveys that adopted schemes such as box-least squares with fixed orbital periods, particularly for systems with low signal to noise.

All four of the co-orbital planet pairs formed in our simulations are mutually inclined and lead to a similar situation to that discussed above. So far, no confirmed co-orbital planets have been found. We note that simulations involving dynamical relaxation within a protoplanetary disc also suggest that 1:1 co-orbital planets are a natural outcome (Cresswell & Nelson 2006, 2008), but in that case the co-orbital pairs are expected to be coplanar and hence would both be detected directly in transit surveys. The strong TTV signal we demonstrated here might provide an explanation of why co-orbital pairs have not been found, and also provide a means of detecting non-coplanar co-orbital systems.

5 COLLISION-INDUCED COMPOSITION CHANGES

Recent analyses of the distribution of planetary radii for planets discovered by Kepler indicate the presence of a valley in the distribution for radii $1.6 \lesssim R_p \lesssim 2$ $R_\oplus$ (Fulton et al. 2017; Fulton & Petigura 2018; Van Eylen et al. 2018). The location of this valley has been widely interpreted as providing evidence that complete photoevaporation of hydrogen–helium envelopes from core-dominated super-Earths has unveiled a population of bodies whose densities are consistent with them having Earth-like compositions (Owen & Wu 2017; Jin & Mordasini 2018). The lack of clear evidence for the solid cores having densities consistent with having significant ice fractions suggests that the observed cores did not migrate to their current locations after formation beyond the ice line. An alternative possibility that we explore here is that

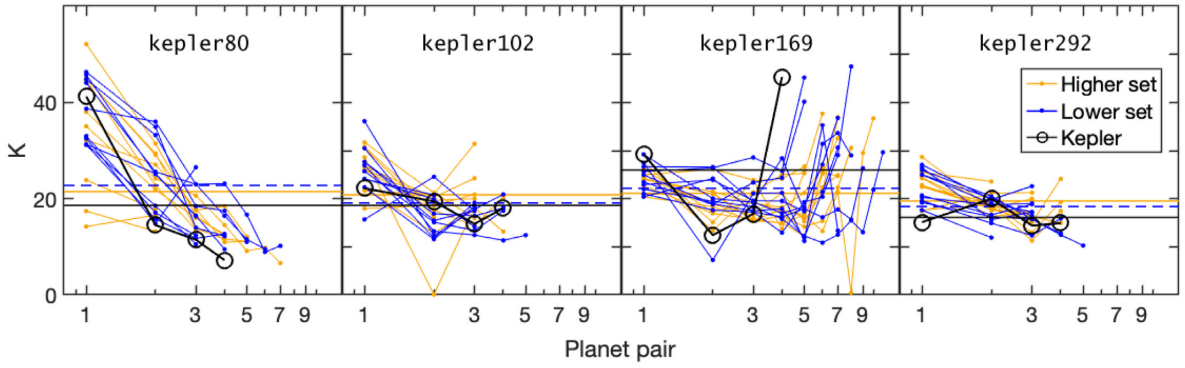

Figure 12. All K-values for neighbouring planet pairs from imperfect collision simulations of (from left to right) `Kepler80`, `102`, `169`, and `292` templates. The orange diamonds are from the higher initial eccentricity set and the blue triangles are from the lower initial eccentricity set. The horizontal lines in each subplot are the mean values of the data in their respective colour (also plotted as solid lines for the higher initial eccentricity set and dashed lines for the lower initial eccentricity set). The black circles denote the K-values of the original planets pairs, as listed in Table 1.

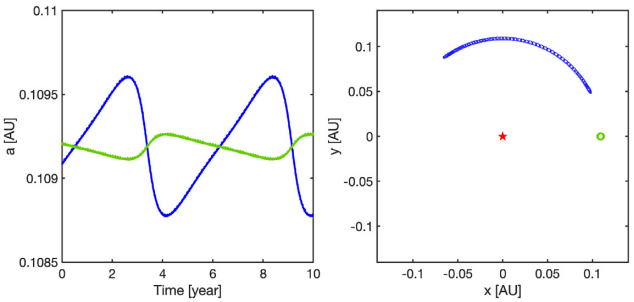

Figure 13. The left-hand panel shows the semimajor axis evolution of the co-orbital planet pair. The right-hand panel shows the orbit trajectory of the same planet pair in a frame that corotates with the planet denoted by the green open circle.

high-energy collisions during giant impacts may have changed the compositions of previously water-rich cores by stripping off the volatile outer layers.

For head-on collisions, the specific collision energy, $Q_{\rm R}$, can be calculated according to

$$Q_{\rm R} = \frac{1}{2}\frac{\mu V_{\rm imp}^2}{M_{\rm Total}}, \tag{19}$$

where the reduced mass $\mu = (M_1 M_2)/(M_1 + M_2)$ (with M_1 and M_2 being the masses of the target and projectile, respectively), $M_{\rm Total}$ is the total mass of the two colliding bodies, and $V_{\rm imp}$ is the relative impact velocity. Stewart & Leinhardt (2009) give a catastrophic disruption threshold energy, $Q^*_{\rm RD}$, which depends on the sizes of the colliding objects and $V_{\rm imp}$. $Q^*_{\rm RD}$ is defined as the energy needed to leave the largest remnant with less than 50 per cent of $M_{\rm Total}$ and is given by the relation

$$Q^*_{\rm RD} = \frac{1}{10^4} R_{C1}^{1.2} V_{\rm imp}^{0.8}, \tag{20}$$

where R_{C1} is the radius of a spherical body containing all of the colliding mass with a density $\rho_1 = 1$ g cm^{-3}, given by

$$R_{C1} = \sqrt[3]{\frac{3M_{\rm Total}}{4\pi\rho_1}}. \tag{21}$$

With the masses of the two colliding bodies known, and the impact velocities measured from the N-body simulations, we can obtain

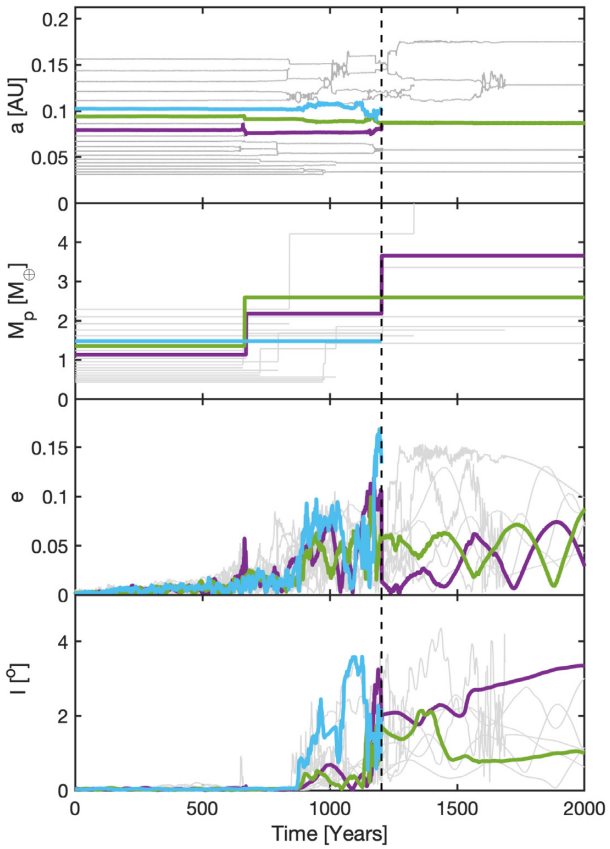

Figure 14. An example of the formation of a co-orbital planet pair by an inelastic collision. Shown are the evolution of the semimajor axes (top panel), planet masses, (second panel) eccentricities (third panel), and inclinations (fourth panel). The time interval shown is the first 2000 yr of the simulation, and the collision occurred after ∼1200 yr (dashed line). The representing three bodies involved in the encounter are marked in blue, green, and purple, where we name them planet-b, planet-g, and planet-p, respectively.

$Q_{\rm R}$ and $Q^*_{\rm RD}$ directly. Marcus et al. (2010) considered collisions involving differentiated bodies, with half of the mass of the colliding planets being water–ice and the other half being rock, and found that the mass fraction of the core of the largest remnant, $M_{\rm core}/M_{\rm lr}$,

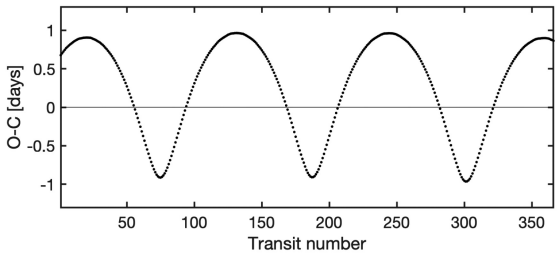

Figure 15. An example synthetic TTV signal for the 1:1 co-orbital planet pair discussed in the text. It shows the difference between the observed and calculated (predicted) times of planet-g's transit events for 10 yr after the end of the formation simulation. A total of 366 transit events are observed within this 10 yr period.

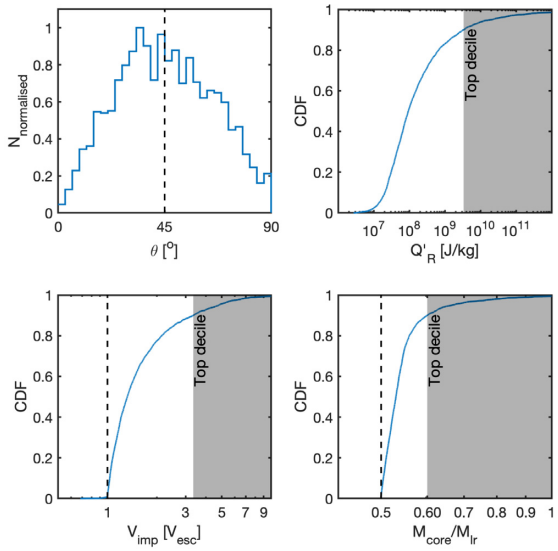

Figure 16. Information concerning collisions occurring across all imperfect accretion simulations. The top left panel shows the distribution of impact angles. The top right panel shows the cumulative distribution of the impact energies, calculated using equation (25). The bottom left panel shows the cumulative distribution of the impact velocities in units of the escape velocity, and the bottom right panel shows the cumulative distribution of the ratio of $M_{\rm core}/M_{\rm lr}$, calculated using equation (27). The grey area in each plot denotes the region where the cumulative number is within 10 per cent of the maximum.

can be fitted by the expression

$$\frac{M_{\rm core}}{M_{\rm lr}} = 0.5 + 0.25\left(\frac{Q_{\rm R}}{Q^*_{\rm RD}}\right)^{1.2}. \quad (22)$$

This power law of $Q_{\rm R}/Q^*_{\rm RD}$ is the best fit from their smoothed particle hydrodynamics simulations.

The upper left panel of Fig. 16 shows the distribution of the recorded impact angles, θ, in all the giant impact events from our imperfect accretion routine. It is clear that the majority of the collisions are not head-on. For a more realistic analysis for the composition changes, we also consider the effect of off-centre collisions. Leinhardt & Stewart (2012) provide a correction to $Q_{\rm R}$ and $Q^*_{\rm RD}$ that allows them to be applied to off-centre collisions by considering the fraction of the projectile mass that directly intersects the target during a collision. The mass fraction of M_2 involved in the collision is defined as α (i.e. $\alpha = M_{2,\rm involved}/M_2$). After defining α, the interacting reduced mass, μ_α, can be calculated by

$$\mu_\alpha = \frac{\alpha M_1 M_2}{\alpha M_2 + M_1}, \quad (23)$$

where α can be calculated directly from the information recorded during the simulations by

$$\alpha = \frac{3R_2\left[R_{\rm Total} - R_{\rm Total}\sin\theta\right]^2 - \left[R_{\rm Total} - R_{\rm Total}\sin\theta\right]^3}{4R_2^3}, \quad (24)$$

where $R_{\rm Total} = R_1 + R_2$, and $\alpha = 1$ when $R_1 - R_2 > R_{\rm Total}\sin\theta$. The specific impact energy with off-centre collision correction, $Q'_{\rm R}$, can then be calculated according to

$$Q'_{\rm R} = \frac{\mu}{\mu_\alpha} Q_{\rm R}. \quad (25)$$

And similarly, the catastrophic disruption threshold energy with off-centre collision correction, $Q'^*_{\rm RD}$, can be calculated by

$$Q'^*_{\rm RD} = \left(\frac{\mu}{\mu_\alpha}\right)^{2-\frac{3\bar{\mu}}{2}} Q^*_{\rm RD}, \quad (26)$$

where $\bar{\mu}$ is the velocity exponent in the coupling parameter (Holsapple & Schmidt 1987; Housen & Holsapple 1990). Leinhardt & Stewart (2012), and its follow-up study by Stewart & Leinhardt (2012), suggested that the range of values of $\bar{\mu}$ is between 0.33 to 0.37. The middle value ($\bar{\mu} = 0.35$) is adopted in equation (26) for our calculations. With the new value of $Q'_{\rm R}$ and $Q'^*_{\rm RD}$ calculated by equations (25) and (26), respectively, the mass ratio between the core and the largest remnant from equation (22) is modified to

$$\frac{M_{\rm core}}{M_{\rm lr}} = 0.5 + 0.25\left(\frac{Q'_{\rm R}}{Q'^*_{\rm RD}}\right)^{1.2}. \quad (27)$$

Our imperfect accretion simulations record all of the data needed to calculate $M_{\rm core}/M_{\rm lr}$, and hence determine whether or not the giant impacts occurring in the simulations would have been likely to lead to significant compositional changes if our protoplanets were differentiated bodies consisting of ~ 50 per cent rock and ~ 50 per cent water–ice, as considered by Marcus et al. (2010). The results of our analysis are shown in Fig. 16. In the upper left panel, the histogram shows the impact angles, which are peaked at the value around 45°, as expected (Shoemaker 1962). The lower left panel records the cumulative distribution of $V_{\rm imp}$ in terms of the mutual surface escape velocity, $V_{\rm esc}$, of all collisions experienced across all of the imperfect accretion simulations. The upper right panel shows the cumulative value of $Q'_{\rm R}$, and the lower right panel shows the resulting estimates of $M_{\rm core}/M_{\rm lr}$ arising from each collision, calculated from equations (25) and (27). The data suggest that only 10 per cent of the giant impacts in our simulations would lead to a greater than 10 per cent mass-loss from the protoplanet, where this mass-loss would correspond to partial stripping of the putative water-rich mantle. It is very uncommon to have a collision that can cause the protoplanet to have a mass-loss of up to 45 per cent (i.e. 90 per cent of the water/ice content), so we conclude that while moderate compositional changes would be likely to have occurred if the Kepler multiplanet systems underwent a final stage of assembly involving giant impacts, the changes would have been insufficient to explain the location of the valley in the distribution of planetary radii discussed above.

6 COLLISION-INDUCED ATMOSPHERIC LOSS

Observations and structure models of exoplanets suggest that many of the low- and intermediate-mass planets observed by

Kepler have hydrogen–helium (H/He) envelopes (e.g. Lopez & Fortney 2014). These H/He envelopes must have been accreted while the planets were embedded in the gaseous protoplanetary disc (e.g. Bodenheimer & Lissauer 2014; Coleman, Papaloizou & Nelson 2017). If dynamical instabilities and giant impacts after the dispersal of the gas disc have played an important role in the final assembly of the super-Earths and mini-Neptunes observed by Kepler, then the envelopes we observe today must have survived the giant impacts. Previous studies have investigated the conditions under which giant impacts can lead to ejection of an envelope, both by the shock that is driven through the envelope during the impact (Genda & Abe 2003; Inamdar & Schlichting 2016; Yalinewich & Schlichting 2019), and because of the intense heating of the core and envelope that occurs when the impact energy is converted to thermal energy during the collision (Biersteker & Schlichting 2019).

Following the discussion in Biersteker & Schlichting (2019), we make the simplifying assumption that the kinetic energy associated with an inelastic collision between two bodies is converted efficiently into thermal energy in the planetary core, and good thermal coupling between the core and envelope ensures that the base of the envelope achieves the same temperature as the core. If this temperature is such that the Bondi radius of the envelope is smaller than the core radius, then we assume that the atmosphere is lost, or is at least severely eroded.

The impact energy, $E_{\rm imp} = 1/2\mu V_{\rm imp}^2$, associated with each collision between two protoplanets is reported by our `symba` simulations. Hence, in a post-processing step, we can determine the distribution of impact energies from our simulations and determine whether or not these are likely to be sufficient to erode any putative envelopes that the planets might possess. The increase of the temperature, ΔT, due to the impact event can be estimated by equating the impact energy to the change in thermal energy in the core that is present after the impact (which has a mass $M_{\rm lr}$):

$$E_{\rm imp} = \eta c_{\rm v} M_{\rm lr} \Delta T, \tag{28}$$

giving

$$\Delta T = \eta \frac{1}{2} \frac{\mu}{M_{\rm lr}} \frac{V_{\rm imp}^2}{c_{\rm v}}. \tag{29}$$

Here, $c_{\rm v}$ is the specific heat capacity of the core, and η is an energy conversion efficiency factor. The impact should lead to an increase of the final temperature of the core after the impact, $T_{\rm c,\,final} = T_{\rm c,\,initial} + \Delta T$, and here we take a conservative approach and assume that the initial core temperature is negligible compared to the final value (i.e. $T_{\rm c,\,initial} \simeq 0$). Assuming that the base of the envelope has the same temperature as the core, the associated Bondi radius becomes

$$R_{\rm B} = \frac{2GM_{\rm lr}}{c_{\rm s}^2} = \frac{2GM_{\rm lr}\mu_{\rm m}}{\gamma k_{\rm B} T_{\rm c,final}}, \tag{30}$$

where $c_{\rm s}$ is the sound speed, $\mu_{\rm m}$ is the mean molecular weight, γ is the adiabatic index, and $k_{\rm B}$ is the Boltzmann constant. We assume that the atmosphere is likely lost due to an impact if $R_{\rm B} \leq R_{\rm core}$.

When calculating the value of ΔT and $R_{\rm B}$, we assume that the envelopes are a mixture of molecular hydrogen and atomic helium with $\mu_{\rm m} = 2.3$u and $\gamma = 7/5$. Previous studies have taken values of the specific heat capacity of the cores of super-Earths and mini-Neptunes in the interval $c_{\rm v} = 500$–$1000\,{\rm J\,kg^{-1}\,K^{-1}}$ (Alfè, Price & Gillan 2001; Valencia et al. 2010; Nettelmann et al. 2011; Lopez, Fortney & Miller 2012). In this study, we adopt the middle value within this range, $c_{\rm v} = 750\,{\rm J\,kg^{-1}\,K^{-1}}$, as in Biersteker & Schlichting (2019).

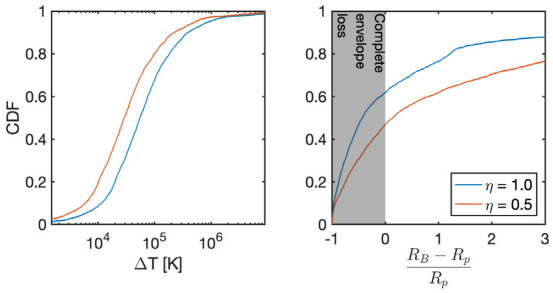

Figure 17. Cumulative distributions of (left-hand panel) ΔT; (right-hand panel) $(R_{\rm B} - R_{\rm p})/R_{\rm p}$ calculated by all the giant impact events in our imperfect collision model simulations. Where $(R_{\rm B} - R_{\rm p})/R_{\rm p} \leq 0$ implies that the Bondi radius is equal to or smaller than the radius of the planet, i.e. complete H/He envelope loss (the grey area). The blue line denotes the value calculated with an energy conversion efficiency of 100 per cent ($\eta = 1$), and the red line denotes the value calculated with the energy conversion efficiency of 50 per cent ($\eta = 0.5$).

The left-hand panel in Fig. 17 shows the cumulative distribution of the post-impact changes in core temperature, ΔT, and the right-hand panel shows the distribution of the quantity $(R_{\rm B} - R_{\rm core})/R_{\rm core}$, such that a negative value implies substantial erosion of the envelope. From the figure, we can see that more than 60 per cent of the collisions in our simulations could lead to envelope loss. These values were obtained by adopting $\eta = 1$ in equation (29), corresponding to 100 per cent efficiency in converting impact kinetic energy into heat. Given that not all collisions are head-on, this is clearly an overestimate, as some of the energy can be converted into rotational energy or be taken away by post-impact debris (Agnor & Asphaug 2004).

Carter, Lock & Stewart (2018) investigated the Moon-forming impact and showed that around half of the impact kinetic energy is converted to internal energy, such that a more realistic figure would be $0.4 < \eta < 0.6$. It is worth noting that in practice, however, in a five-planet system that was initially composed of 20 protoplanets, each remaining planet after the final assembly stage would have experienced three collisions on average, suggesting that significant atmospheric erosion should occur in super-Earth systems whose final assembly involves giant impacts.

Clearly, a more sophisticated approach is required to give a better quantitative estimate of the population of planets that are left with significant H/He envelopes after such a period of evolution. Such a calculation would provide one means of determining whether or not the observed population of super-Earths did indeed form via giant impacts. Even if the impacts themselves are unable to completely erode the envelopes, the remnant envelopes will be left in a bloated state and would therefore be more susceptible to photoevaporation by high-energy radiation from the central star, as considered in the models of Owen & Wu (2017) and Jin & Mordasini (2018), for example. Hence, in the future, it will be important to consider the evolution of envelopes during and after the giant impact phase to determine whether the resulting population of planets agrees with the observations.

7 SYNTHETIC OBSERVATION OF THE FINAL PLANETARY SYSTEMS

The ability of any photometric observation of a planetary system to detect transits of all system members depends on the mutual inclinations of the planets. In addition, for any given planet with

semimajor axis a, orbiting around a star with radius R_*, the probability of detecting a transit from a random viewing position scales as R_*/a, such that more distant planets around smaller stars are more difficult to detect. Based on these considerations, a meaningful comparison between the outcomes of planetary formation simulations and transit surveys, such as the one carried out by Kepler, must involve synthetic observation of the simulated planetary systems.

Broadly speaking, the masses, orbital period ratios, and planetary separations (as measured by the K-values) resulting from the N-body simulations show reasonable agreement with the inferred properties of the Kepler systems we have used as templates when setting up the initial conditions of the simulations. Here, we are interested in whether or not the distributions of the multiplicities of the simulated planetary systems, and the period ratios between neighbouring planets, when synthetically observed, agree with an appropriate subset of the Kepler systems. If such an agreement was obtained, then it would support the hypothesis that the observed Kepler systems are all intrinsically high-multiplicity systems with mutual inclinations similar to those that arise in the N-body simulations, which in turn would imply that the final assembly of the Kepler systems likely arose from a population of protoplanets that underwent dynamical instabilities and giant impacts, as considered in our N-body simulations. In addition, recent analyses have indicated that planets that are members of multiple systems have a statistically significant different eccentricity distribution compared to planets that are observed to be single (e.g. Xie et al. 2016; Mills et al. 2019). We test whether this difference is matched by our simulations when synthetically observed.

7.1 Observed multiplicities

Following the approach of Johansen et al. (2012), we consider that the relative numbers of one-planet, two-planet, three-planet, up to seven-planet systems that are detected when the simulation outcomes are synthetically observed from 100 000 randomly chosen viewing locations, isotropically distributed with respect to each host star. Using the observed numbers of one-planet, two-planet, three-planet, etc. systems, we then define a Transit Multiplicity Ratio (abbreviated to TMR hereafter) as follows:

$$\mathrm{TMR}(i,\,j) = \frac{\text{Number of } i\text{-planet systems}}{\text{Number of } j\text{-planet systems}}, \tag{31}$$

where i and j represent the numbers of planets detected during each of the synthetic observations.

For a comparison with the TMR values obtained from the N-body simulations, we take a subset of the Kepler Planet Candidates with the following cuts applied to the orbital periods, P, and planetary radii, R_p, so that the Kepler sample roughly matches the simulation outcomes: 3 d $\leq P \leq$ 100 d and 1 $\mathrm{R}_\oplus \leq R_\mathrm{p} \leq$ 4 $\mathrm{R}_\oplus$. In addition, to crudely account for the fact that the detection efficiency of Kepler decreases for small planets with longer orbital periods, we also required the planet to have a radius greater than the value given by $R_\mathrm{min} = 0.60(P/1\ \mathrm{d})^{0.111}\ \mathrm{R}_\oplus$ when undertaking the synthetic observations. Incorporating this limit on the planet radius excluded around 20 per cent of our final planets, but made essentially no difference to the TMRs obtained from the synthetic transit observations.

The TMR values obtained are shown in Fig. 18, where the coloured histograms show the values obtained from each of the different sets of N-body simulations, the blue horizontal bars show the mean values averaged over the different simulation sets, and the black horizontal bars show the TMRs from the Kepler data. The left-hand panel shows TMRs for two-planet:one-planet systems, three-planet:two-planet systems, four-planet:three-planet systems, etc., and the right-hand panel shows TMRs for n-planet systems relative to two-planet systems, where n is an integer running between 3 and 7. The results are very clear: The simulations consistently overproduce high-multiplicity systems relative to low-multiplicity systems by a factor of between 1.5 and 2 compared to the Kepler systems. One reason for this is that the planet–planet scattering, leading to increases in the mutual inclinations of planetary orbits during the N-body simulations, does not increase the mutual inclinations sufficiently for agreement to be reached. The N-body simulation outcomes have mutual inclinations that are too low, with the RMS value obtained from the inclinations plotted in Fig. 8 being $\langle I \rangle = 2.05^\circ$.

In their earlier studies of multiplicity ratios, Johansen et al. (2012) and Tremaine & Dong (2012) suggest that mean mutual inclinations of $\langle\, I \rangle \simeq 5^\circ$ would be sufficient to provide agreement between their models and the Kepler data when comparing the relative numbers of three-planet and two-planet systems. This indicates that a factor of 2 increase in inclinations in our model systems would likely lead to much better agreement with the Kepler systems, given the factor of $\sim$2 discrepancy shown between the TMRs shown in Fig. 18. Even more recently, Izidoro et al. (2019) and Carrera et al. (2019) have presented N-body simulations that provide much better agreement with the Kepler TMRs than our results do. In the case of the Izidoro et al. (2019) study, this improved agreement arises in part because they simulate the formation of more massive planetary systems than we do, leading to more effective gravitational scattering, but in addition their simulations result in a number of systems with lower intrinsic multiplicities compared to our simulations.

7.2 Period ratios

The CDF of the period ratios between neighbouring planets obtained from the synthetic observation of the simulation outcomes is shown in Fig. 19, along with that for the full set of Kepler planets that make up our comparison sample, and a subset of that sample for which the maximum period ratio is 3:1. This figure should be compared with Fig. 10, which shows the CDF of the intrinsic period ratios obtained from the simulations before being synthetically observed. This comparison demonstrates the importance of undertaking synthetic observations to mimic transit surveys, as the two distributions of period ratios are quite different from one another. We see from Fig. 19 that we obtain a significant increase in the frequency of period ratios $>$2 when undertaking the synthetic observations, as planet pairs on mutually inclined orbits are not observed to simultaneously transit. However, it is also clear that the Kepler data still show a significant excess of large period ratios compared to the simulations, and in general the Kepler systems are more separated than the simulated systems. We also note that we recover the fact that the Kepler systems also show a significant excess of small period ratios compared to the simulations, discussed already in Section 3.2.4.

One curious feature of the CDF shown in Fig. 19 is the flattening observed close to the location of the 2:1 resonance, which is reminiscent of the similar feature seen in the Kepler data due to there being a small deficit of planets at the 2:1 resonance location. This is not observed so strongly in the CDF of the intrinsic period ratios shown in Fig. 10, so we have examined the possibility that it arises

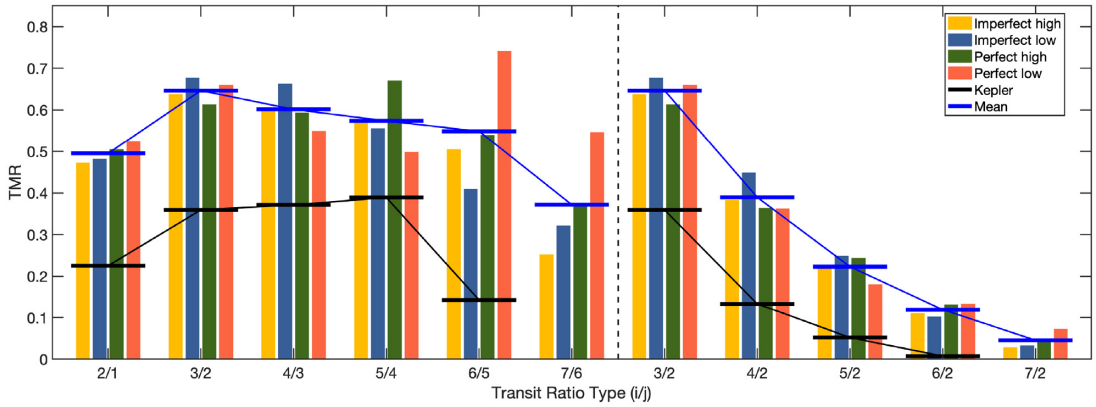

Figure 18. Synthetic TMR from all four sets of our simulations. The yellow and blue bars denote the high and low initial eccentricity value simulations with imperfect accretion, respectively; the green and red bars denote the high and low initial eccentricity simulations with perfect accretion, respectively. The black horizontal lines show the observed Kepler TMRs (as of 17/10/2018) and the blue horizontal lines show the mean values of the simulated TMRs.

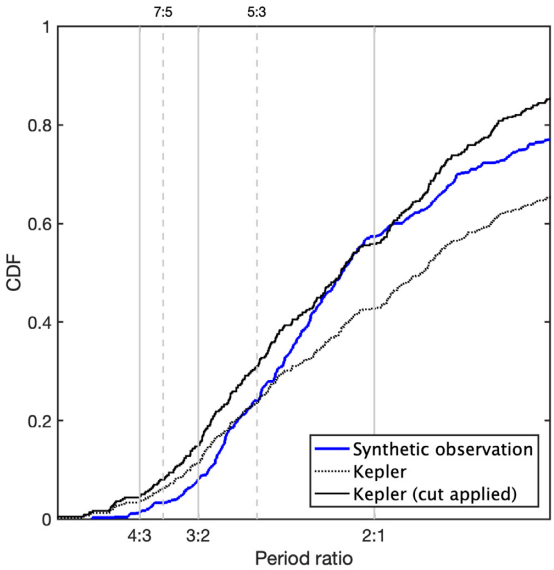

Figure 19. CDFs of the period ratios obtained from the synthetic observations of the simulations, and for a comparison the CDFs of period ratios obtained from our comparison sample of the Kepler data.

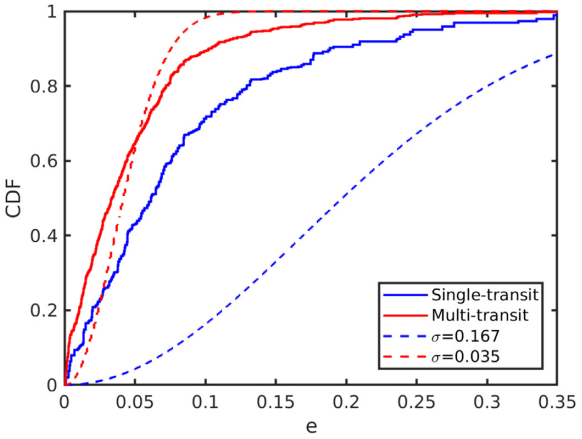

Figure 20. CDFs of the eccentricities obtained from the synthetic observations of the simulations, and for a comparison the CDFs of eccentricities drawn from Rayleigh distributions with eccentricity parameters $\sigma_e = 0.035$ and 0.167.

here because mutual inclinations of planet pairs are increased near to this resonance. Plotting mutual inclinations against period ratios, however, showed no significant feature close to the 2:1 resonance, so for now this feature remains unexplained.

7.3 Eccentricity distributions

The CDFs of the eccentricities of the synthetically observed planets are shown in Fig. 20, where the solid lines represent either systems observed to be singles or those observed to be multiples. The dashed lines show the CDFs for eccentricities drawn from a Rayleigh distribution with eccentricity parameters $\sigma_e = 0.035$ and 0.167, which are the distributions and values for the observed Kepler multiple and single systems from Mills et al. (2019). While it is clear that the simulations produce single planets with systematically larger eccentricities than the planets in multiplanet systems because the singles are from systems that have undergone stronger scattering than the multiples, it is also clear that the simulations do not provide a good match to the observationally inferred distributions of eccentricities from Mills et al. (2019). In particular, the singles would need to be much more eccentric to match the observationally inferred distribution, and it is not at all clear that *N*-body simulations of the type presented here could fit the appropriate distribution of eccentricities, while also adopting planetary masses in line with those thought to make up the Kepler compact systems of super-Earths (such as shown in Fig. 21). On the other hand, although the distribution from multiple systems is not particularly well fitted by the Rayleigh distribution, the range of eccentricities obtained is in much better agreement compared to those obtained for single transiting systems. Using a maximum likelihood estimation, and scanning through different values of σ_e, we find that an *assumed* Rayleigh distribution with parameter $\sigma_e = 0.049$ provides the best fit to the multiple systems arising from the simulations. In future work, we will examine fitting the observed eccentricity distributions with the results of *N*-body simulations that consider different scenarios to those presented here.

Under conditions of strong scattering, the perturbed radial velocity of a planet relative to a circular Keplerian orbit, v_r, should correspond approximately to the escape velocity from the perturbing body. Assuming typical planet masses and radii $\bar{M}_p$ and $\bar{R}_p$,

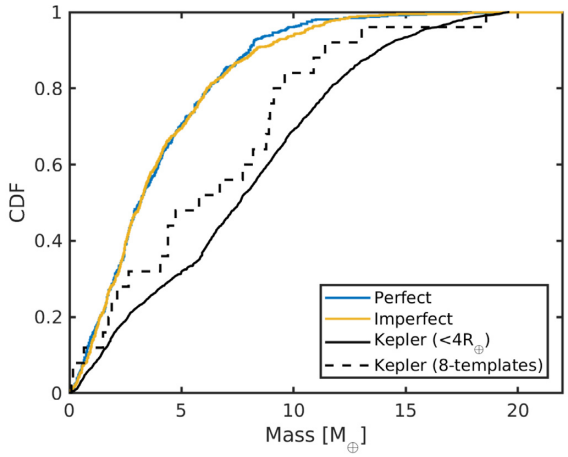

Figure 21. Cumulative distributions of the planet masses obtained from the simulations and inferred from the Kepler data using the mass–radius relation described in the text.

respectively, we have $v_r \sim \sqrt{2G\bar{M}_p/\bar{R}_p}$. For small eccentricities, $e \sim v_r/v_k$, where v_k is the Keplerian velocity. From the CDF of simulated planet masses in Fig. 21, the median planet mass $\bar{M}_p \sim 2.5$ M$_\oplus$ and the corresponding radius $\bar{R}_p \sim 1.56$ R$_\oplus$. For planets orbiting at $a_p \sim 0.1$ au, the eccentricity expected from strong scattering is $e \sim 0.15$. The median eccentricity for single planets synthetically observed in the simulations is $e \sim 0.07$, and approximately 20 per cent of planets have eccentricities above the strong scattering value of $e \sim 0.15$. Hence, strong scattering contributes significantly to the eccentricity distribution, but weaker scattering events and collisional damping result in the majority of planets having smaller eccentricities. Finally, it is expected that the mean inclination $\bar{i} \sim \bar{e}/2$ after dynamical relaxation (Kokubo 2005). For $\bar{e} \sim 0.07$, the expected mean inclination is $\bar{i} \sim 2^\circ$, very similar to the mean value observed in the simulations, as discussed in Section 3.2.3.

Finally, we comment that for strong scattering it is expected that the resulting eccentricities will scale as $e \sim \sqrt{M_p}$. The discrepancy between the median eccentricity of the simulated single planets and the Rayleigh distribution with $\sigma_e = 0.167$, shown in Fig. 20, is about a factor of 3 (∼0.07 versus ∼0.2). Hence, to generate this shift would require an increase in the masses of the planets by a factor of ∼9. The CDFs for the planet masses from the simulations, and those inferred from the Kepler data, are shown in Fig. 21, and there we observe about a factor of 3 discrepancy between the simulated planets and the Kepler planets. Hence, it is not clear at present whether or not strong scattering of planets that appear to be singles in the Kepler data can account for the inferred eccentricity distribution of these planets as derived by Mills et al. (2019).

8 DISCUSSION AND CONCLUSIONS

8.1 Recap of simulation set-up

We have presented the results of *N*-body simulations of *in situ* planetary system formation. These examine whether or not the final assembly of the Kepler compact multiplanet systems, and perhaps the wider population of Kepler planets, can be explained by a scenario in which a large number of orbiting protoplanets experience dynamical instability after the gas disc has dispersed, and accrete through giant impacts, until long-term stable systems emerge. Our approach to creating initial conditions was to take eight of the known Kepler five-planet systems, and to use these as templates for producing systems of 20 protoplanets, whose total mass was the same as the original Kepler systems (under the assumption of a particular mass–radius relation). For each Kepler template, we considered two different distributions of initial eccentricities and inclinations, a 'high set' for which the maximum values $[e_{max}, I_{max}] = [0.02, 0.01]$, and a 'low set' for which $[e_{max}, I_{max}] = [0.002, 0.001]$. For each of these sets, we also adopted two different routines for handling collisional growth: a traditional, perfect accretion model that assumes hit-and-stick collisions; an imperfect accretion model that allows for a range of collision outcomes based on the prescriptions of Leinhardt & Stewart (2012). One of our main results is that the simulation outcomes had almost no detectable dependence on the collision model adopted, and this is because the systems we explored did not dynamically excite themselves sufficiently for collisions to be highly disruptive. This is in agreement with the recent study by Mustill et al. (2018). Consideration of more massive planetary systems, however, may lead to outcomes that depend on the collision model as the enhanced gravitational scattering may lead to higher collision velocities.

8.2 Recap of main results

All of the *N*-body simulations resulted in dynamical instability and collisions between protoplanets. The mean time-scale for collisions to occur was approximately 3×10^5 orbital periods, measured at the centre of the annulus containing the protoplanets, indicating that the systems had time for dynamical relaxation to occur during the process of collisional growth. 90 per cent of collisions occurred within 1 Myr, and we ran the simulations for a total of 10 Myr.

The final outcomes of the simulations generally showed good agreement with the Kepler systems we used as templates, indicating that the procedure adopted for setting up the simulations gave rise to plausible initial conditions. In particular, the final distributions of planet masses, orbital period ratios, separations between neighbouring planets, and intrinsic multiplicities showed good agreement with the templates on average. Notably, our simulations failed to produce any one-planet or two-planet systems. This suggests that if single- or double-planet systems are intrinsically common among the Kepler systems, as has been suggested (Johansen et al. 2012), then the formation scenario presented here cannot explain them. If the single transiting planets are instead members of multiplanet systems whose mutual inclinations prevent all planets being observed, however, then final assembly through planet–planet scattering and giant impacts remains plausible (Carrera et al. 2019; Izidoro et al. 2019). Similarly, widely spaced pairs of neighbouring planets with large period ratios are very difficult to explain in a model where the initial distribution of protoplanets is smooth and continuous. For these latter systems, it would appear necessary for the initial distributions of planetary building blocks to contain localized concentrations of protoplanets in order to produce the large period ratios seen in the Kepler data. Alternatively, some other process, such as migration, which can cause planets to move relative to one another, would need to be included in the models to explain the well-separated planet pairs that have been observed.

We undertook synthetic transit observations of the final planetary systems formed in the simulations. We counted the relative numbers of one-planet, two-planet, three-planet, ..., seven-planet systems detected by the synthetic observations, and compared this with an appropriate subset of the Kepler data that matched the parameters of the model planetary systems. We found that the simulated systems

overproduce, by about a factor of 2, the numbers of high-multiplicity versus low-multiplicity systems compared to the Kepler systems. This arises in part because the excitation of mutual inclinations in our simulations is too small by about a factor of 2, and also because our planetary systems produce too few low-multiplicity systems. We have examined the distributions of the masses of the planets obtained in the simulations, and find that these are smaller than the typical inferred masses of the planets in the Kepler data set (considering planets with radii $< 4\,R_\oplus$). Fig. 21 shows the CDFs of the planet masses from the simulations and the Kepler planets, and it shows: (i) the Kepler systems we chose as templates have moderately smaller masses than the Kepler data set as a whole we are comparing against; (ii) the simulations produce too many low-mass planets compared to both the templates and the Kepler systems as a whole, because systems with higher multiplicity than 5 are formed. It is likely that by choosing more massive discs of protoplanets as initial conditions, the resulting planet masses, and the enhanced scattering they would experience, would lead to final systems more in agreement with the Kepler data, both in terms of inferred planet masses and in terms of the distribution of multiplicities, because of the larger mutual inclinations that would have been excited. This may also result in eccentricity distributions that are in better agreement with the observations than we obtained in the simulations presented here. Alternatively, if final period of dynamical instability in multiplanet systems is initiated when the planets are essentially fully formed, rather than when the system consists of numerous low-mass protoplanets, then it may be possible to achieve higher eccentricities and mutual inclinations because the scattering may be stronger and collisions may occur less frequently.

8.3 Recent relevant planet formation studies

In their recent study, Izidoro et al. (2019) were able to construct a population of planetary systems, which when synthetically observed provided good agreement with the Kepler multiplicity distribution. This was achieved by combining simulations that resulted in resonant chains of planets that became dynamically unstable with simulations in which the resonant chains remained stable. It is noteworthy that only 5 per cent of the included planetary systems were intrinsically one-planet systems, with most of the rest being multiple systems in which the mutual inclinations typically exceeded 4°. In an earlier study, Moriarty & Ballard (2016) undertook a study of the multiplicity distributions arising from *N*-body simulations of planet formation, adopting a range of surface density profiles and masses in their initial discs of protoplanets and planetesimals. As with our simulations, theirs also formed planetary systems with intrinsic multiplicities $N_p \geq 3$, and by suitably combining their different simulation results they were able to produce a population of planets that agreed with the Kepler distribution of multiplicities when their simulated systems were synthetically observed. Hence, it appears that combining a range of initial conditions for planet formation simulations, which ultimately result in dynamical instabilities and giant impacts, can lead to systems that collectively provide mutual inclinations and intrinsic multiplicities that agree with observations when their transits are simulated.

8.4 Intrinsic multiplicities from RV studies

The agreement between these simulations and the observations raises an important question: Are essentially all planetary systems intrinsically multiple systems, even when observed to be singles by transit surveys? And if so, what is the underlying multiplicity distribution? Transit surveys cannot directly answer this. The detection of TTVs in apparently single-planet systems discovered by Kepler, however, shows that a number of these planets have neighbours close to mean motion resonances (Kane et al. 2019). In addition, the fact that the eccentricities of single planets appear to be systematically higher than in multiple planet systems (Mills et al. 2019) indicates that a number of apparently single planets have likely been subject to gravitational scattering, and hence are members of multiplanet systems. Radial velocity surveys can, in principle, detect nearby companions in compact multiplanet systems, assuming modest mutual inclinations, although they are constrained by limits imposed by spectral resolution, instrument stability, and stellar variability, and numerous compact multiplanet systems have been discovered by this method (e.g. Mayor et al. 2011). None the less, there are hints in the data that super-Earths do not always come as members of compact multiple systems. For example, the recently discovered super-Earth orbiting with a period of 233 d around Barnard's star indicates a lack of close orbiting planets with similar masses in that system (Ribas et al. 2018), and certainly none that became anchored at the inner edge of the protoplanetary disc during their formation, as often occurs in *N*-body simulations of planet formation that involve pebble drift or planet migration. Similarly, Proxima b, orbiting with a period of 11 d does not appear to have closely neighbouring planets of similar masses (Anglada-Escudé et al. 2016). While these are only individual examples, they indicate that not all planetary systems are compact multiples. Future high-precision RV surveys targeted at characterizing the multiplicities of short-period super-Earth systems will have the power to determine whether or not final assembly of planetary systems via dynamical instability is the dominant mode of planet formation, or if instead a substantial population of relatively isolated planets exists that cannot be explained by the giant impact formation route.

8.5 Compact non-resonant systems

Furthermore, compact systems of super-Earths, such as Kepler-11 (Mahajan & Wu 2014), that contain planets on low-eccentricity orbits, and which are apparently close to instability, are also difficult to assemble via dynamical instabilities and giant impacts. Kepler-11 appears to have been assembled in a highly dissipative environment, presumably in a gaseous protoplanetary disc – which is supported by the low densities of some of the planets (Lissauer et al. 2013), but none of the planet pairs are in mean motion resonance. Hence, while dynamically quiet formation in a disc seems necessary, the lack of resonances indicates that disc-driven migration may not have played an important role in this system. We note, however, that recent analyses of single- and multiple-planet migration in inviscid protoplanetary discs by McNally et al. (2019b) and McNally, Nelson & Paardekooper (2019a) lead to more complex migration behaviour of planets than has been found to traditionally occur in viscous discs. Hence, the formation of resonant chains is not a foregone conclusion in inviscid discs, and such an environment may provide a way of forming systems such as Kepler-11. A reasonable conclusion is that the observational evidence appears to indicate that a number of different pathways are required for the final assembly of planetary systems.

8.6 Co-orbital systems

Approximately 1 per cent of our simulations gave rise to pairs of planets in apparently long-term stable 1:1 co-orbital resonances,

occupying both tadpole and horseshoe orbits. These normally form early in the simulations, when the numbers of protoplanets are high and the planetary systems are undergoing strong planet–planet interactions. The co-orbital pairs arise as a result of three-body encounters removing the requisite energy and angular momentum from a pair of planets such that the co-orbital configuration can form. These co-orbital planet pairs occur with equal frequency in the perfect and imperfect collision model simulations, indicating that the treatment of collisions has no effect on their formation. In spite of intensive searches through the Kepler data, no co-orbital planet systems have been found. We note, however, that there are just over 100 Kepler systems with known multiplicity ≥ 3 that fall within the parameter ranges covered by our simulations, so a 1 per cent occurrence rate, which would agree with the simulations results, leads to an expectation that just one co-orbital system would have been found. Hence, the current data set is too small to determine if the observed planets indeed formed from a large number of protoplanets undergoing dynamical relaxation and collisions, leading to co-orbital pairs forming with an efficiency of ~ 1 per cent per system. Future missions, such as PLATO, will monitor many more stars than Kepler (Rauer et al. 2014), and hence will place more stringent constraints on the formation histories of compact multiplanet systems.

8.7 Composition changes and envelope loss

Recent observations have indicated the presence of a valley in the distribution of planet radii for short-period Kepler planets (Fulton et al. 2017; Fulton & Petigura 2018; Van Eylen et al. 2018), and models of envelope photoevaporation suggest that the position of the valley is most easily explained if the cores of super-Earths that are subject to photoevaporation are rocky rather than volatile rich (Owen & Wu 2017; Jin & Mordasini 2018). In this context, we examined whether or not high-energy collisions during our simulations could significantly modify the compositions of the final planets relative to the initial protoplanets. In post-processing, we used the scaling relations between collision energies and compositional changes presented by Marcus et al. (2010), and examined whether or not high-energy collisions occurred frequently enough that they could remove a large fraction of water-rich mantles of colliding, differentiated protoplanets whose initial compositions were 50 per cent rock and 50 per cent water–ice. The results of this analysis suggest that collisional stripping of water-rich mantles cannot explain the fact that the apparently naked cores observed by Kepler have an Earth-like composition, instead of a mixture of rock and water–ice. It seems unlikely, therefore, that these now naked cores formed exterior to the ice line and migrated to their current locations. Using a similar analysis, we also examined whether or not the impact energies of collisions between protoplanets could be sufficient to remove any H/He envelopes they might possess. Our simple analysis suggests that ~ 30 per cent of collisions occurring in the simulations could remove gaseous envelopes, such that planets experiencing multiple collisions would have a high probability of losing their envelopes completely. Further modelling of this process could place significant constraints on the collisional history of the observed population of super-Earths and mini-Neptunes. Compared to the scenario examined here in which a large number of protoplanets undergo collisional accretion during the final assembly of exoplanet systems, the exoplanet data likely point to an origin in which systems of fewer, essentially fully formed planets undergo dynamical relaxation after dispersal of the gas disc in order to produce the observed orbital architectures, while undergoing fewer collisions in order to maintain the gaseous envelopes possessed by a large number of the observed exoplanets.

In future work, we will present simulations with a significantly broader range of initial conditions, to assess the conditions under which dynamical instabilities in multiplanet systems may have contributed to the final stage assembly of the observed short-period super-Earths and mini-Neptunes.

ACKNOWLEDGEMENTS

This research utilized Queen Mary's Apocrita HPC facility, supported by QMUL Research-IT.[3] RPN acknowledges support from the Science and Technology Funding Council (STFC) through the grants ST/P000592/1 and ST/M001202/1.

REFERENCES

Agnor C., Asphaug E., 2004, ApJ, 613, L157
Alfè D., Price G. D., Gillan M. J., 2001, Phys. Rev. B, 64, 045123
Anglada-Escudé G. et al., 2016, Nature, 536, 437
Barclay T., Quintana E. V., Adams F. C., Ciardi D. R., Huber D., Foreman-Mackey D., Montet B. T., Caldwell D., 2015, ApJ, 809, 7
Batalha N. M. et al., 2013, ApJS, 204, 24
Biersteker J. B., Schlichting H. E., 2019, MNRAS, 485, 4454
Bodenheimer P., Lissauer J. J., 2014, ApJ, 791, 103
Borucki W. J. et al., 2010, Science, 327, 977
Borucki W. J. et al., 2011, ApJ, 736, 19
Burke C. J. et al., 2014, ApJS, 210, 19
Burns J. A., Lamy P. L., Soter S., 1979, Icarus, 40, 1
Carrera D., Ford E. B., Izidoro A., 2019, MNRAS, 486, 3874
Carter P. J., Lock S. J., Stewart S. T., 2019, preprint (arXiv:1912.04936)
Chambers J. E., 1999, MNRAS, 304, 793
Chiang E., Laughlin G., 2013, MNRAS, 431, 3444
Coleman G. A. L., Nelson R. P., 2014, MNRAS, 445, 479
Coleman G. A. L., Nelson R. P., 2016, MNRAS, 457, 2480
Coleman G. A. L., Papaloizou J. C. B., Nelson R. P., 2017, MNRAS, 470, 3206
Cossou C., Raymond S. N., Hersant F., Pierens A., 2014, A&A, 569, A56
Coughlin J. L. et al., 2016, ApJS, 224, 12
Cresswell P., Nelson R. P., 2006, A&A, 450, 833
Cresswell P., Nelson R. P., 2008, A&A, 482, 677
Dermott S. F., Murray C. D., 1981a, Icarus, 48, 1
Dermott S. F., Murray C. D., 1981b, Icarus, 48, 12
Duncan M. J., Levison H. F., Lee M. H., 1998, AJ, 116, 2067
Fressin F. et al., 2013, ApJ, 766, 81
Fulton B. J., Petigura E. A., 2018, AJ, 156, 264
Fulton B. J. et al., 2017, AJ, 154, 109
Funk B., Schwarz R., Dvorak R., Roth M., 2011, MNRAS, 410, 455
Funk B., Dvorak R., Schwarz R., 2013, Celest. Mech. Dyn. Astron., 117, 41
Genda H., Abe Y., 2003, Icarus, 164, 149
Guess A. W., 1962, ApJ, 135, 855
Hadden S., Lithwick Y., 2014, ApJ, 787, 80
Haisch Jr. K. E., Lada E. A., Lada C. J., 2001, ApJ, 553, L153
Hansen B. M. S., Murray N., 2012, ApJ, 751, 158
Hansen B. M. S., Murray N., 2013, ApJ, 775, 53
Hellary P., Nelson R. P., 2012, MNRAS, 419, 2737
Holsapple K. A., Schmidt R. M., 1987, J. Geophys. Res., 92, 6350
Housen K. R., Holsapple K. A., 1990, Icarus, 84, 226
Inamdar N. K., Schlichting H. E., 2016, ApJ, 817, L13
Izidoro A., Ogihara M., Raymond S. N., Morbidelli A., Pierens A., Bitsch B., Cossou C., Hersant F., 2017, MNRAS, 470, 1750

[3] http://doi.org/10.5281/zenodo.438045

Izidoro A., Bitsch B., Raymond S. N., Johansen A., Morbidelli A., Lambrechts M., Jacobson S. A., 2019, preprint (arXiv:e-print)
Jin S., Mordasini C., 2018, ApJ, 853, 163
Johansen A., Davies M. B., Church R. P., Holmelin V., 2012, ApJ, 758, 39
Kane M., Ragozzine D., Flowers X., Holczer T., Mazeh T., Relles H. M., 2019, AJ, 157, 171
Kokubo E., 2005, in Knežević Z., Milani A., eds, IAU Colloq. 197: Dynamics of Populations of Planetary Systems. Cambridge Univ. Press, Cambridge, p. 41
Lambrechts M., Morbidelli A., Jacobson S. A., Johansen A., Bitsch B., Izidoro A., Raymond S. N., 2019, A&A, 627, A83
Leinhardt Z. M., Stewart S. T., 2012, ApJ, 745, 79
Levison H. F., Duncan M. J., 1994, Icarus, 108, 18
Lissauer J. J. et al., 2011a, ApJS, 197, 8
Lissauer J. J. et al., 2011b, Nature, 470, 53
Lissauer J. J. et al., 2013, ApJ, 770, 131
Lopez E. D., Fortney J. J., 2014, ApJ, 792, 1
Lopez E. D., Fortney J. J., Miller N., 2012, ApJ, 761, 59
MacDonald M. G. et al., 2016, AJ, 152, 105
McNally C. P., Nelson R. P., Paardekooper S.-J., 2019a, MNRAS, 489, L17
McNally C. P., Nelson R. P., Paardekooper S.-J., Benítez-Llambay P., 2019b, MNRAS, 484, 728
Mahajan N., Wu Y., 2014, ApJ, 795, 32
Marcus R. A., Sasselov D., Stewart S. T., Hernquist L., 2010, ApJ, 719, L45
Matsumoto Y., Kokubo E., 2017, AJ, 154, 27
Matsumoto Y., Nagasawa M., Ida S., 2012, Icarus, 221, 624
Mayor M. et al., 2011, preprint (arXiv:1109.2497)
Mills S. M., Howard A. W., Petigura E. A., Fulton B. J., Isaacson H., Weiss L. M., 2019, AJ, 157, 198
Moriarty J., Ballard S., 2016, ApJ, 832, 34
Mullally F. et al., 2015, ApJS, 217, 31
Mustill A. J., Davies M. B., Johansen A., 2018, MNRAS, 478, 2896
Nettelmann N., Fortney J. J., Kramm U., Redmer R., 2011, ApJ, 733, 2
Ogihara M., Morbidelli A., Guillot T., 2015, A&A, 578, A36
Owen J. E., Wu Y., 2017, ApJ, 847, 29
Petigura E. A., Howard A. W., Marcy G. W., 2013, Proc. Natl. Acad. Sci., 110, 19273
Petrovich C., Malhotra R., Tremaine S., 2013, ApJ, 770, 24
Poynting J. H., 1903, MNRAS, 64, 1
Press W. H., Teukolsky S. A., Vetterling W. T., Flannery B. P., 1992, Numerical Recipes in FORTRAN. The Art of Scientific Computing, 2nd edn. Cambridge Univ. Press, Cambridge
Rauer H. et al., 2014, Exp. Astron., 38, 249
Ribas I. et al., 2018, Nature, 563, 365
Robertson H. P., 1937, MNRAS, 97, 423
Rowe J. F. et al., 2014, ApJ, 784, 45
Rowe J. F. et al., 2015, ApJS, 217, 16
Shallue C. J., Vanderburg A., 2018, AJ, 155, 94
Shoemaker E. M., 1962, Interpretation of Lunar Crater. Physics and Astronomy of the Moon. Academic Press Inc., NewYork, USA
Stewart S. T., Leinhardt Z. M., 2009, ApJ, 691, L133
Stewart S. T., Leinhardt Z. M., 2012, ApJ, 751, 32
Tabachnik S. A., Evans N. W., 2000, MNRAS, 319, 63
Terquem C., Papaloizou J. C. B., 2007, ApJ, 654, 1110
Thompson S. E. et al., 2018, ApJS, 235, 38
Tremaine S., Dong S., 2012, AJ, 143, 94
Valencia D., Ikoma M., Guillot T., Nettelmann N., 2010, A&A, 516, A20
Van Eylen V., Agentoft C., Lundkvist M. S., Kjeldsen H., Owen J. E., Fulton B. J., Petigura E., Snellen I., 2018, MNRAS, 479, 4786
Weiss L. M., Marcy G. W., 2014, ApJ, 783, L6
Wiegert P. A., Holman M. J., 1997, AJ, 113, 1445
Wisdom J., Holman M., 1991, AJ, 102, 1528
Wolfgang A., Rogers L. A., Ford E. B., 2016, ApJ, 825, 19
Wu Y., Lithwick Y., 2013, ApJ, 772, 74
Wu D.-H., Zhang R. C., Zhou J.-L., Steffen J. H., 2019, MNRAS, 484, 1538
Xie J.-W. et al., 2016, Proc. Natl. Acad. Sci., 113, 11431
Yalinewich A., Schlichting H., 2019, MNRAS, 486, 2780
Zhu W., Petrovich C., Wu Y., Dong S., Xie J., 2018, ApJ, 860, 101

APPENDIX A: PLANETESIMAL RING FRAGMENTATION

For the imperfect collision simulations, which adopted the collision model from Leinhardt & Stewart (2012), approximately 10 per cent of our simulations experienced at least one supercatastrophic collision, leading to the formation of a ring composed of collision debris in the form of planetesimals. This ring was often confined to the inner most regions close to the star, where collision velocities can reach their highest values, and this led to large numbers of particles needing to be integrated using small time-step sizes. In order to overcome this problem, we developed a scheme for reducing the

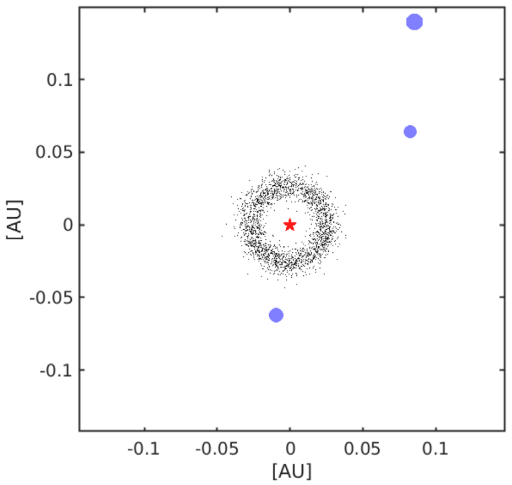

Figure A1. An example of an inner ring from one of our simulations, where the small black dots are the position of the inner ring objects. The blue circles denote the planets with their size proportional to their mass. The centre red pentagram is the position of the host star. Viewed from the top of the system, all bodies are orbiting the host star in an anticlockwise direction. Parameter information about this inner ring is listed in Fig. A2 and Table A1.

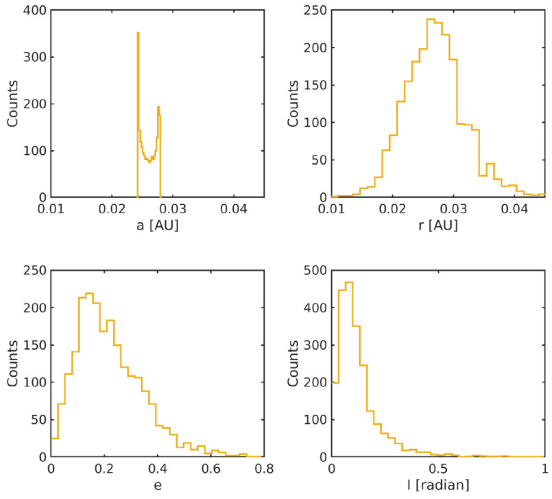

Figure A2. Counting distribution of all inner ring object parameters. Where it shows the distribution of the (top left) semimajor axis, (top right) distance, *r*, from the host star, (bottom left) eccentricities, and (bottom right) inclinations.

Table A1. Fragmentation ring parameters for `Kepler55_low_06`, displayed in Fig. A1.

N	$a_{\rm in}$ (au)	$a_{\rm out}$ (au)	$\langle a \rangle$ (au)	$\langle e \rangle$	$\langle I \rangle$ (rad)
2177	0.0241	0.0283	0.0260	0.2213	0.1272

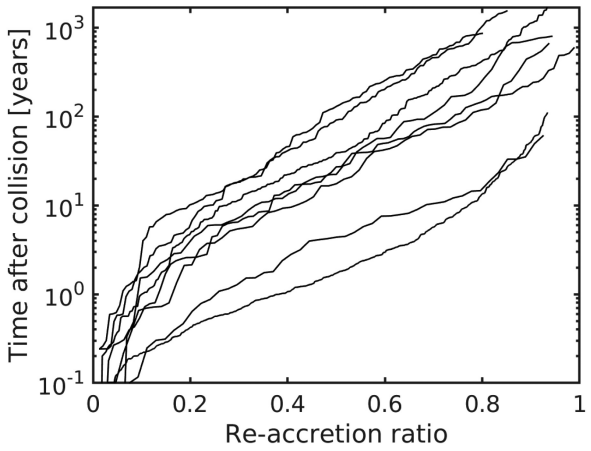

Figure A3. Time since collision versus the fraction of debris particles remaining since the collision for eight collision events selected from the simulations.

masses of the ring particles on a time-scale corresponding to their collision time-scales. Then, once the mass of the ring reaches negligible values, the ring particles could be removed from the simulations, since the planetesimals would then be ground down to dust, which would be removed in reality by the Poynting–Robertson effect for grain sizes between 1 mm to 1 μm (Poynting 1903; Robertson 1937; Guess 1962) or radiation pressure for grains smaller than 1 μm (Burns, Lamy & Soter 1979). When there is a fragmentation ring detected between the innermost big body and the host star, we apply the following step during the simulation.

The total number of bodies in the ring, N, the mean semimajor axis, $\langle a \rangle$, eccentricity, $\langle e \rangle$, inclination, $\langle I \rangle$, and semimajor axis of the innermost and outermost bodies in the ring ($a_{\rm out}$ and $a_{\rm in}$) can be found from the simulations. These can be used to calculate the collision time in the ring, $\tau_{\rm coll}$, according to

$$\tau_{\rm coll} = \frac{1}{n\sigma \langle v \rangle}, \tag{A1}$$

where n is the number density given by

$$n \approx \frac{N}{2\pi \left(a_{\rm out}^2 - a_{\rm in}^2\right) \langle a \rangle \langle I \rangle}. \tag{A2}$$

The velocity dispersion $\langle v \rangle$ is given by

$$\langle v \rangle \approx \langle v_{\rm k} \rangle \sqrt{\langle e^2 \rangle + \langle I^2 \rangle}, \tag{A3}$$

where $\langle v_{\rm k} \rangle$ is the mean Keplerian velocity of the objects in the ring. The collision cross-section is simply

$$\sigma = \pi R_{\rm p}^2. \tag{A4}$$

Having obtained the collision time, we then decrease the mass of the ring particles according to

$$m_{\rm p}(t) = m_{\rm p}(t_0) {\rm e}^{-(t-t_0)/\tau_{\rm coll})}, \tag{A5}$$

where t_0 is the time of ring formation, and after 15 e-folding times we remove the ring particles, since their masses are then negligible.

Fig. A1 shows the ring formed in one of our simulations. Fig. A2 shows the parameters of the ring shown in Fig. A1, and Table A1 lists the ring parameters. We can see 2177 bodies with masses ∼0.0015 $M_\oplus$ concentrated between 0.01 and 0.05 au. Applying the parameters of the ring listed in Table A1 to equations (A1), we get $\tau_{\rm coll} = 2.12$ yr, leading to rapid removal of the ring.

We note that Mustill et al. (2018) also include an imperfect accretion model in their simulations, and immediately remove all small debris particles after they are formed because of the small time-scale for collisions and collisional grinding versus the re-accretion time-scale of the debris on to nearby protoplanets. We have examined the re-accretion time-scale for debris particles in our simulations, and find that after a debris cloud is generated the time-scale for half of the debris particles generated to be re-accreted is between ∼2 and ∼100 yr, as shown in Fig. A3. This is considerably shorter than the re-accretion time-scale of 30 000 yr estimated by Mustill et al. (2018), but perhaps comparable to or longer than the typical grinding time-scales for debris clouds generated during collisions. This suggests that a realistic model for the evolution of post-collision debris should allow a fraction of it to re-accrete while the other fraction is ground down and removed by radiation pressure. Incorporating such a model, however, goes beyond the scope of this paper.

APPENDIX B: SURFACE DENSITY FITTING MODEL

Table B1 shows all the coefficients adopted to fit the surface density, $\Sigma_{\rm fit}$, together with the type of fitting model chosen from the models described in Section 2.3. The choice of fitting model was made by selecting the one that gave the best least-squares fit.

Table B1. Surface density fitting model for the eight Kepler templates. For model details, see equation (13).

System template	Fitting model	c_1	c_2	c_3	c_4
`Kepler55`	Power law	1.047×10^{-1}	−2.488	73.80	/
`Kepler80`	Polynomial	-1.687×10^{7}	2.597×10^{6}	-1.097×10^{5}	1.917×10^{3}
`Kepler84`	Polynomial	2.062×10^{5}	-9.379×10^{4}	1.142×10^{4}	-1.507×10^{2}
`Kepler102`	Fourier series	1.042×10^{2}	57.58	37.81	60.55
`Kepler154`	Polynomial	6.073×10^{4}	-3.512×10^{4}	5.303×10^{3}	−25.78
`Kepler169`	Exponential	5.233×10^{2}	−17.72	0	/
`Kepler292`	Power law	29.21	9.643×10^{-1}	0	/
`Kepler296`	Power law	9.924×10^{-1}	−2.082	0	/

APPENDIX C: SIMULATION OUTPUTS FOR INDIVIDUAL TEMPLATES

This section provides the simulation outcomes from all system templates that were not shown in the main body of the paper: `Kepler55, 84, 154, and 296` (imperfect collision simulations) and all eight templates for the perfect collision simulations.

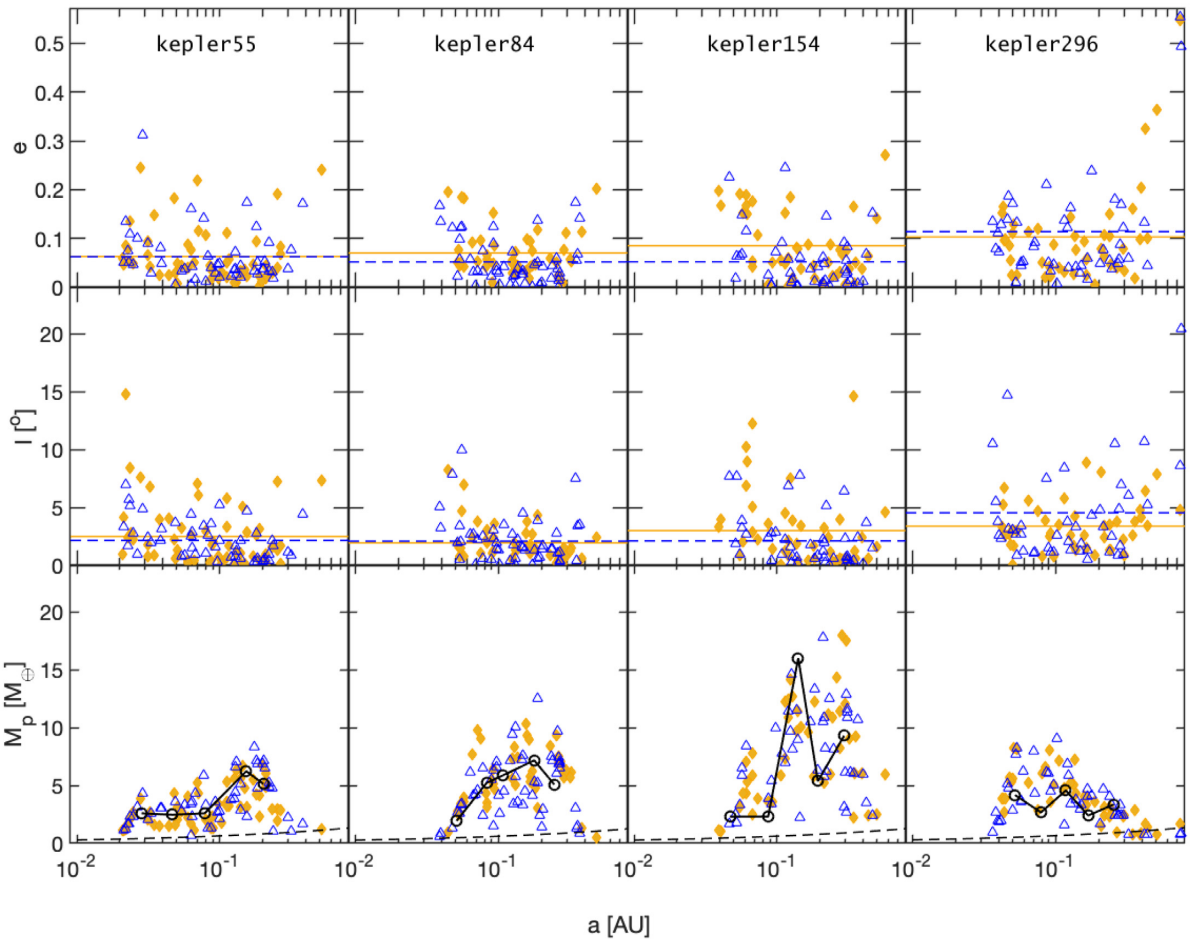

Figure C1. Same plot as Fig. 7 but for the imperfect Kepler-55, 84, 154, and 296 templates.

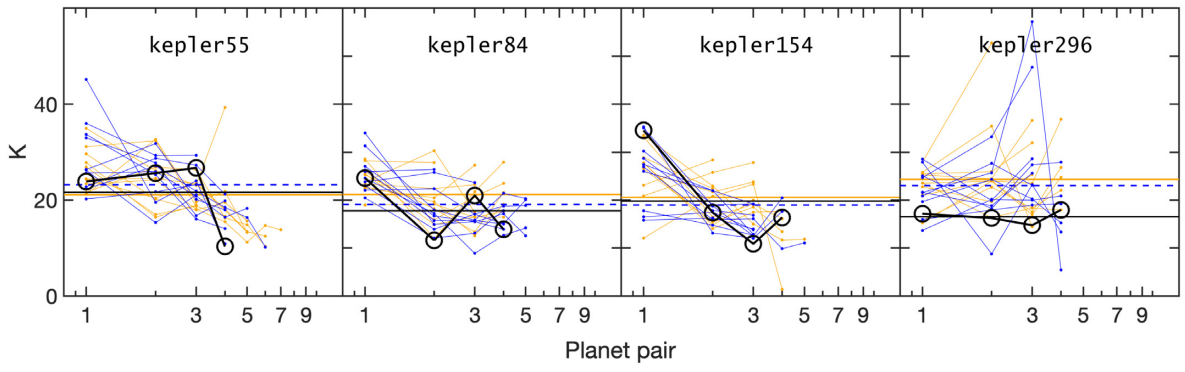

Figure C2. Same plot as Fig. 12 but for the imperfect `Kepler55, 84, 154, and 296` templates.

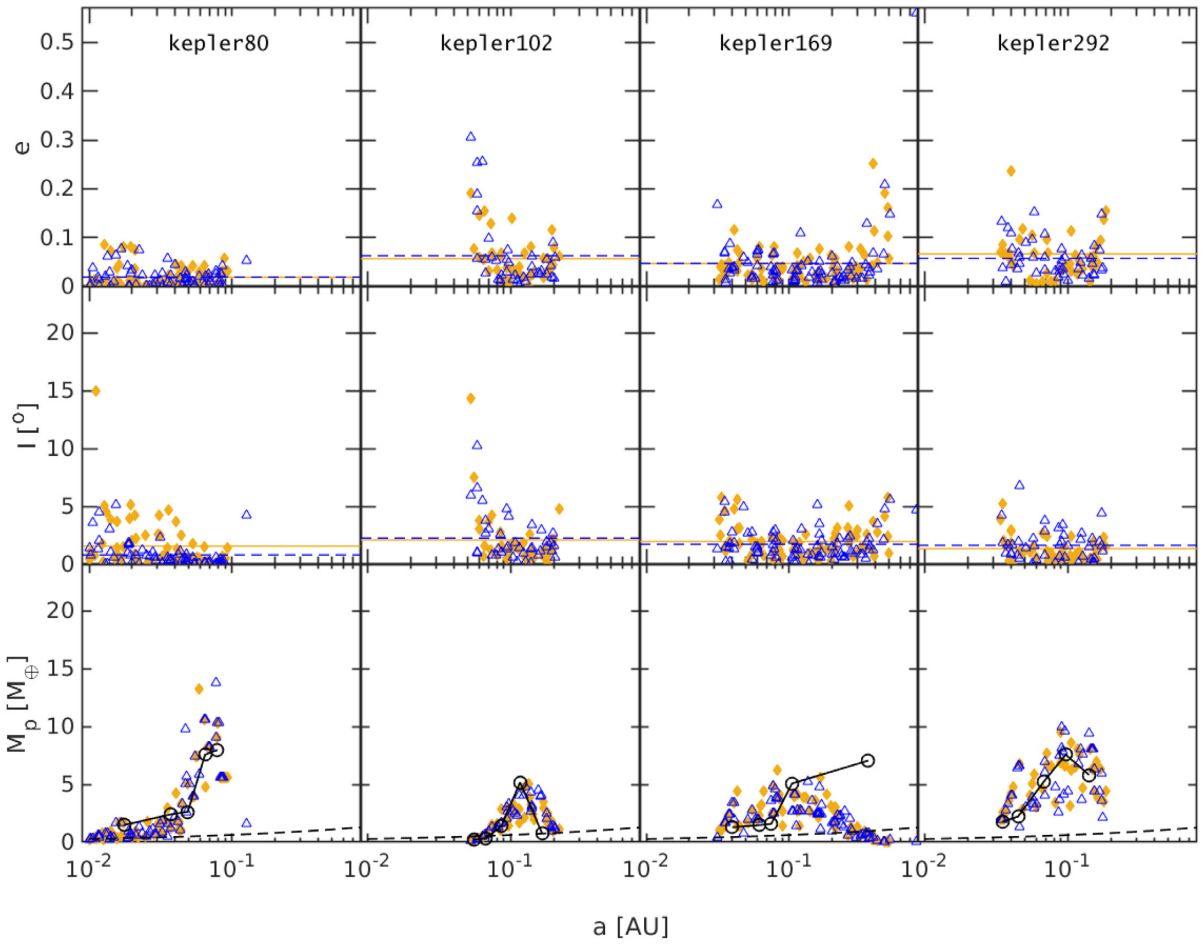

Figure C3. Same plot as Fig. 7 but for the perfect `Kepler80`, `102`, `169`, and `292` templates.

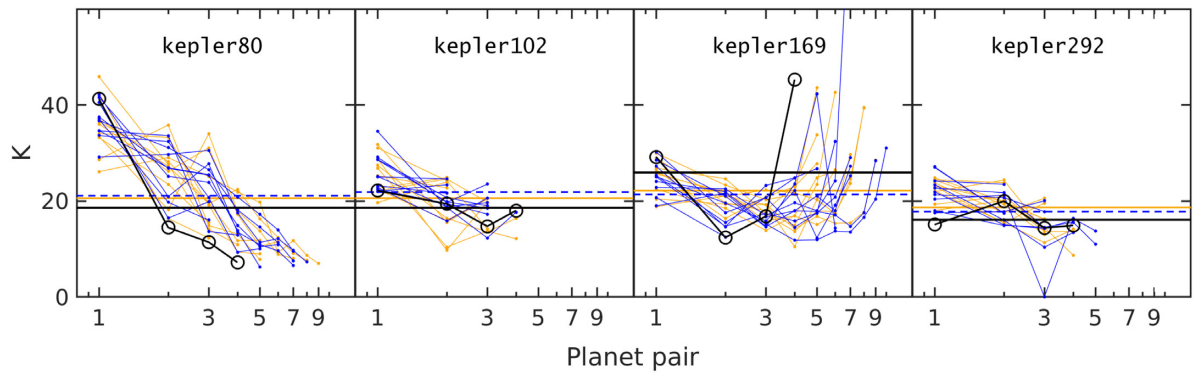

Figure C4. Same plot as Fig. 12 but for the perfect `Kepler80`, `102`, `169`, and `292` templates.

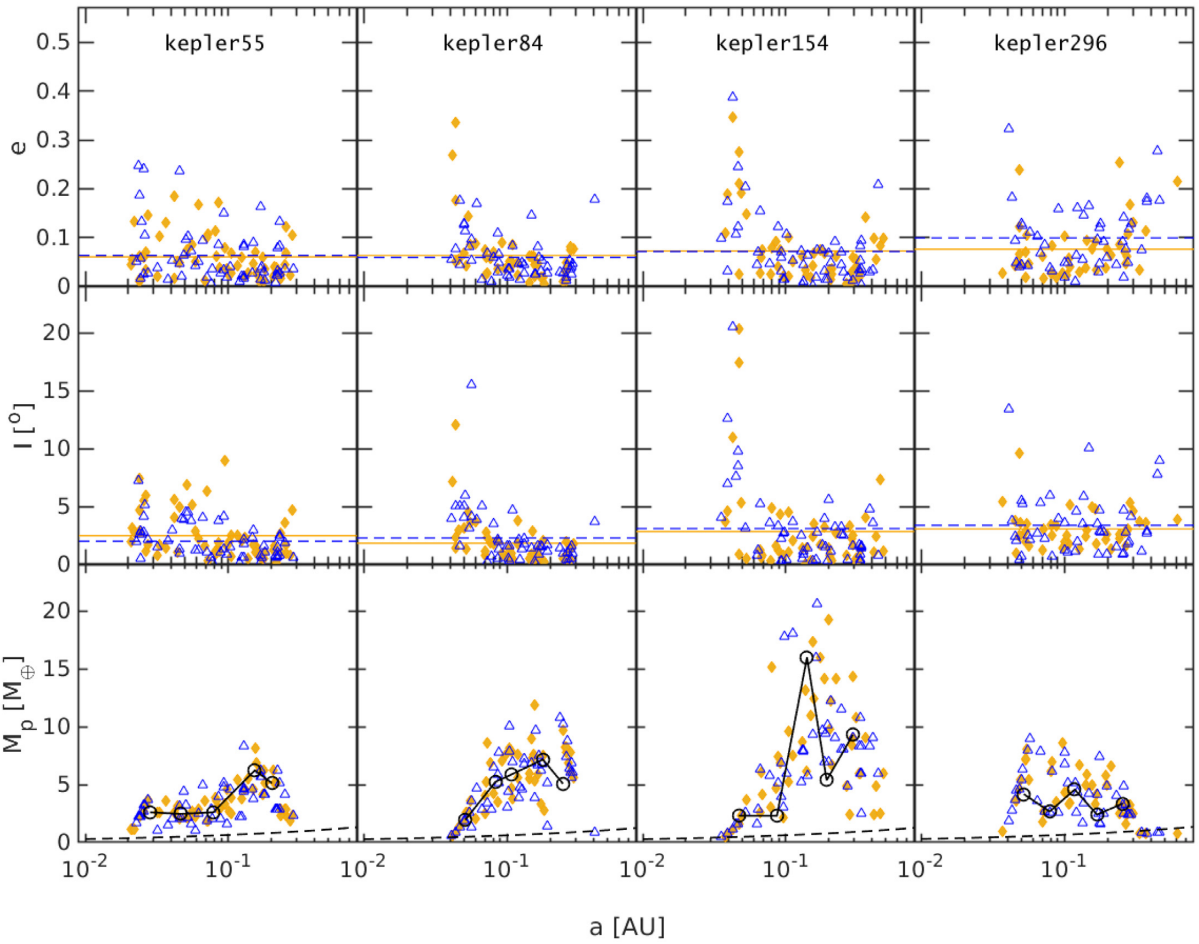

Figure C5. Same plot as Fig. 7 but for the perfect `Kepler55`, `84`, `154`, and `296` templates.

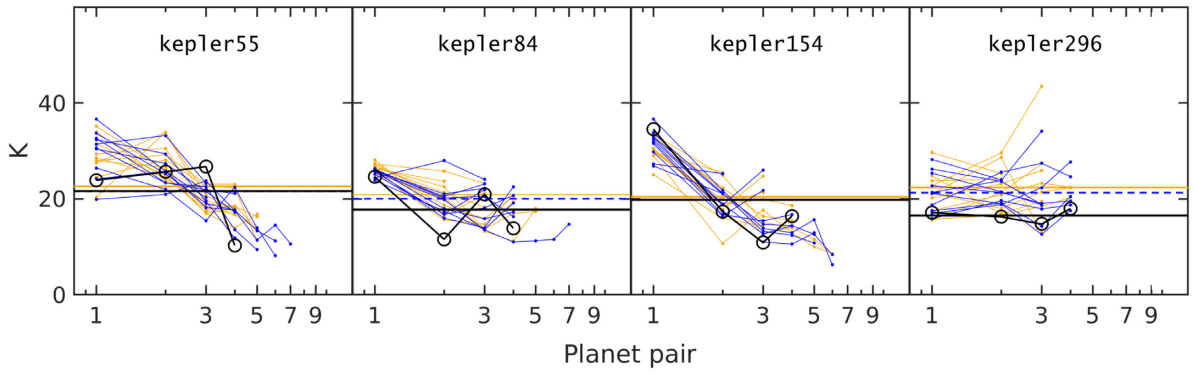

Figure C6. Same plot as Fig. 12 but for the perfect `Kepler55`, `84`, `154`, and `296` templates.

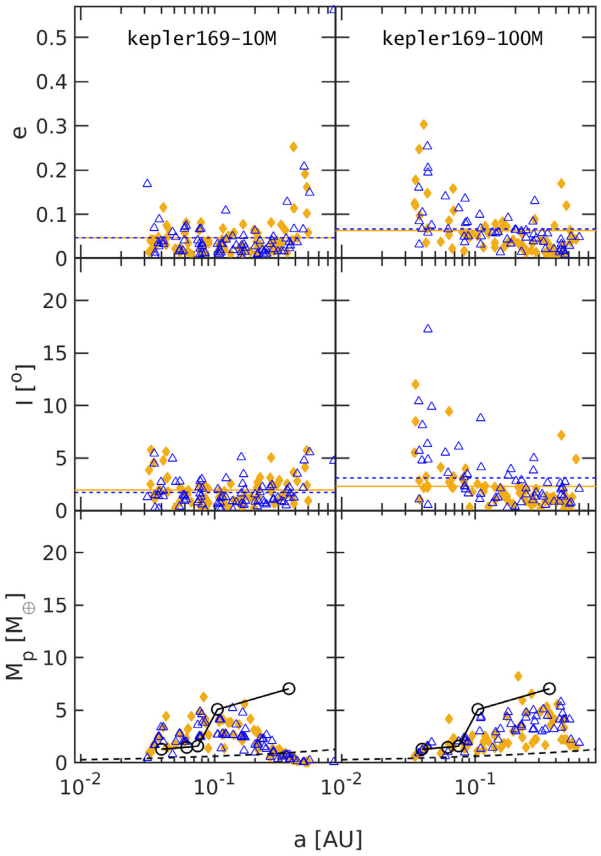

Figure C7. Similar to Fig. 7 but for the comparison of template `Kepler169` (perfect routine) after running 10 and 100 Myr.

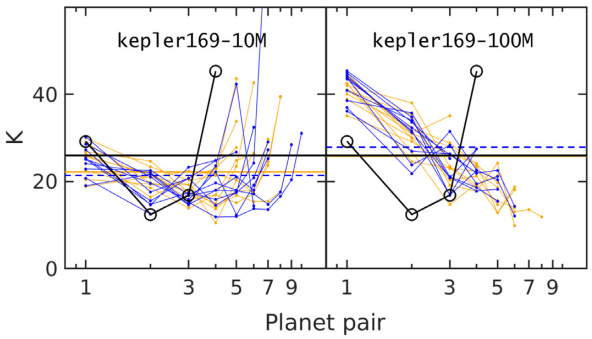

Figure C8. Similar to Fig. 11 but for the comparison of template `Kepler169` (perfect routine) after running 10 and 100 Myr.

This paper has been typeset from a TEX/LATEX file prepared by the author.